Asymmetric retinal direction tuning predicts optokinetic eye movements across stimulus conditions

Scott C. Harris[1,2]* and Felice A. Dunn[1]*

1. Department of Ophthalmology, University of California, San Francisco, San Francisco, CA 94143, USA
2. Neuroscience Graduate Program, University of California San Francisco, San Francisco, CA 94158, USA

*Corresponding Authors, Scott.Harris@ucsf.edu, Felice.Dunn@ucsf.edu

ABSTRACT

Across species, the optokinetic reflex (OKR) stabilizes vision during self-motion. OKR occurs when ON direction-selective retinal ganglion cells (oDSGCs) detect slow, global image motion on the retina. How oDSGC activity is integrated centrally to generate behavior remains unknown. Here, we discover mechanisms that contribute to motion-encoding in vertically-tuned oDSGCs, and leverage these findings to empirically define signal transformation between retinal output and vertical OKR behavior. Specifically, we demonstrate that motion encoding in vertically-tuned oDSGCs is contrast-sensitive and asymmetric for oDSGC types that prefer opposite directions. These phenomena arise from the interplay between spike threshold nonlinearities and differences in synaptic input weights, including shifts in the balance of excitation and inhibition. In behaving mice, these neurophysiological observations, along with a central subtraction of oDSGC outputs, accurately predict the direction and magnitude of vertical OKR across stimulus conditions. Thus, asymmetric synaptic input across competing sensory input channels can critically shape behavior.

31 **INTRODUCTION**

32

33 From humans to insects, a wide range of organisms depend on visual cues to navigate
34 the world. When these animals respond to incoming visual information by enacting motor plans,
35 however, relative motion is created between the eye and the visual scene. Such motion, termed
36 "retinal slip," has the potential to corrupt subsequent vision and threaten survival.

37 To compensate for this possibility, the optokinetic reflex (OKR) is a highly conserved visual
38 behavior that performs retinal image stabilization across an impressive range of species
39 (including invertebrates[1], reptiles, amphibians, fish, birds, and all mammals, including mice and
40 humans, reviewed by ref. [2]). OKR consists of visually-evoked, compensatory eye movements (or
41 head movements in some species) that offset the slow, global image motion generated by self-
42 movement[3]. In most species, OKR is also well known to change across stimulus conditions.
43 Adjustments to stimulus contrast, color, location, velocity, or spatial frequency, for example, can
44 elicit distinct OKR patterns[4–11]. Nonetheless, neurophysiological mechanisms for such
45 phenomena are largely missing.

46 Anatomically, the pathways that underlie OKR in mammals are well defined (reviewed by
47 refs. [2,3,12,13]). Starting in the retina, a dedicated class of biological motion detectors known as ON
48 direction-selective retinal ganglion cells (oDSGCs) encode the slow global image motion that
49 occurs during retinal slip. Classic work identified three types of oDSGCs that each maximize their
50 firing rate in response to a particular cardinal direction of stimulus motion (i.e., up/superior,
51 down/inferior, and nasal/anterior)[14,15]. A recent study also identified a fourth oDSGC type in mouse
52 that encodes temporal/posterior motion[16]. As signals from oDSGCs depart the retina, they avoid
53 typical retinal projection nuclei such as the superior colliculus and lateral geniculate nucleus.
54 Instead, axons from vertically- and horizontally-preferring oDSGCs course along dedicated
55 retinofugal tracts to a set of midbrain nuclei known collectively as the accessory optic system.
56 Vertically-tuned oDSGCs terminate exclusively in, and comprise the sole retinal inputs to, the

57 medial and lateral terminal nuclei (MTN and LTN)[12,17–22] (but see Discussion and ref. [23]) - though
58 in mice, LTN is engulfed within MTN[17,21,24,25]. Here, their inputs are likely integrated into a single
59 velocity signal that reflects the vertical component of retinal slip. This information is then relayed
60 deeper into the brainstem where corresponding eye movements are enacted. Likewise,
61 horizontally-tuned oDSGCs exclusively target the nucleus of the optic tract/dorsal terminal
62 nucleus (NOT/DTN) where their signals are similarly integrated to ultimately generate the
63 horizontal component of OKR[17,24]. While correlations have been recognized between the
64 physiological properties of oDSGCs and OKR - particularly a matched speed tuning[26] - little is
65 known about how signals from multiple oDSGC types are integrated to generate OKR across
66 varying stimulus conditions[12,27].

67 Here, we reveal a general mechanism by which OKR may be generated across a range
68 of stimulus statistics. To do so, we focus primarily on a single parameter that is known to affect
69 OKR: motion direction. In many species - including both humans[28–31] (but see ref. [32]) and mice[21]
70 - OKR is more robust in response to superior than inferior motion. We aim to illuminate the
71 biological mechanism underlying this asymmetry in order to reveal more general processes by
72 which OKR may be differentially generated across stimulus conditions. Focusing on the direction-
73 sensitivity of vertical OKR is methodologically strategic in that (1) it limits the source of possible
74 neurophysiological mechanisms to functions of only the vertical OKR pathway, and (2) unlike
75 horizontal OKR, which relies on interhemispheric communication and mirror-image motion signals
76 from each eye[2,17,33], vertical OKR can be studied unilaterally. Our results indicate that the
77 behavioral asymmetry between superior and inferior OKR is linked to differences in the direction
78 tuning properties of oDSGCs that prefer superior and inferior motion. These physiological
79 differences arise from a shift in the balance of excitatory and inhibitory (E/I) synaptic inputs across
80 cell types, along with nonlinear transformations associated with spike thresholding. More
81 generally, we demonstrate that the tuning properties of vertically-tuned oDSGCs are uniquely
82 sensitive to such changes in synaptic input weights and show how this sensitivity can account for

83 changes to OKR across multiple stimulus conditions in behaving mice. As a whole, this work
84 reveals a neurophysiological mechanism underlying gaze stabilization and natural vision
85 throughout the seeing world.
86
87
88 **RESULTS**
89
90 **Superior OKR is more robust than inferior OKR**
91
92 Across species, superior motion generates a more robust OKR than inferior motion (e.g.
93 cat[33–35], chicken[36], monkey[37], human[28–31]). In mice, this phenomenon has been reported
94 anecdotally in juvenile animals[21]. To investigate if an asymmetry between superior and inferior
95 OKR exists in adult mice, we designed a behavioral rig to accurately evoke and quantify vertical
96 OKR in head-fixed animals (**Fig 1a-b**, Methods)[38]. Eye movements were measured in response
97 to vertically-drifting, full-field gratings that have been used previously to evoke OKR[19,21,24,39].
98 Across all adult mice, superior- and inferior-drifting gratings generated distinct, but reproducible
99 eye movements: while superior gratings elicited repetitive slow, upward drifting eye movements
100 ("slow nystagmus") interleaved with frequent resetting saccades in the opposite direction ("fast
101 nystagmus") (**Fig 1c**), inferior gratings tended to reliably drive only an initial slow nystagmus
102 immediately following stimulus onset, after which fast nystagmuses were infrequent and eye
103 position changed minimally (**Fig 1d**). To quantify these differences, we isolated periods of slow
104 and fast nystagmus post hoc by extracting saccadic eye movements from the raw eye position
105 trace. Superior stimuli elicited more frequent fast nystagmuses than did inferior stimuli (**Fig 1e**).
106 In addition, the total distance traveled during slow nystagmus was greater for superior stimuli (**Fig**
107 **1f**). These results demonstrate that vertical OKR is asymmetric in adult mice.

108 Despite the stark asymmetry between superior and inferior OKR in response to
109 unidirectional drifting gratings, quantifying OKR gain (ratio of eye velocity to stimulus velocity)
110 under these conditions presented challenges due to variability in the OKR waveform across
111 stimulus directions (**Fig 1c-d**). To better quantify gain, we designed a second stimulus in which a
112 grating oscillated sinusoidally between superior and inferior motion while retaining a constant
113 average position. In every animal subject, this oscillating grating evoked sequential superior and
114 inferior slow nystagmuses that were phase-locked to the stimulus (**Fig 1g-h, j**). Removing fast
115 nystagmuses from the eye trace (**Fig 1h**) revealed that gain tended to be higher during the
116 superior phase compared to the inferior phase of individual oscillations (**Fig 1i**). This bias was
117 reflected by an average offset of vertical eye position in the superior direction over the course of
118 a single stimulus oscillation (**Fig 1j**). Taken together, these results demonstrate that superior
119 motion drives a more robust OKR than inferior motion.
120
121 **Superior and Inferior oDSGCs have distinct direction tuning properties**
122
123 While behavioral asymmetries between superior and inferior OKR could arise anywhere
124 along the vertical OKR pathway, a plausible neurophysiological substrate is at the level of the
125 retina where the pathways that encode superior and inferior motion have yet to converge. Further,
126 because the ganglion cells that encode superior motion ("Superior oDSGCs") and inferior motion
127 ("Inferior oDSGCs") together serve as an input bottleneck for the remainder of the pathway, any
128 physiological asymmetry between these cell types will propagate to behavior unless specifically
129 corrected for by subsequent circuitry (see Discussion). Thus, we hypothesized that the behavioral
130 asymmetry between superior and inferior OKR may result from physiological differences between
131 Superior and Inferior oDSGCs.
132 To probe oDSGCs involved in vertical OKR, we made central injections of a fluorescent
133 retrograde tracer into their central target, MTN (**Fig 2a, S1**). This approach labeled an average of

134 667±16 retinal ganglion cells (RGCs; N=17 retinas), distributed evenly across each quadrant of
135 the contralateral retina (**Fig 2b, S1**). We investigated the direction tuning properties of MTN-
136 projecting RGCs by making cell-attached recordings from labeled cells while presenting a drifting
137 bar stimulus that moved slowly (10°/s) across the retina in 8 directions (**Fig 2c**). Importantly, this
138 stimulus was comparable to the grating stimuli used to evoke vertical OKR in behaving animals,
139 i.e. equivalent cycle width, wavelength, and speed to the unidirectional gratings. The majority
140 (94.76%) of retrogradely labeled cells were direction-selective and preferred either dorsal-to-
141 ventral (n=116 of 286) [i.e., Superior oDSGCs, because these cells detect superior motion in
142 visual space after accounting for inversion of the image by the eye's optics (**Fig 2d**)] or ventral-
143 to-dorsal (i.e., Inferior oDSGCs, n=155 of 286) motion on the retina (**Fig 2e**). In agreement,
144 mosaic analyses indicated that retrogradely labeled cells likely consisted of two RGC types (**Fig**
145 **S1**). Both Superior and Inferior oDSGCs invariably had baseline firing rates of approximately 0hz
146 (spikes/s: Sup. 0.0134±0.006; Inf. 0.0338±0.016; p=0.13 Sup. vs. Inf.). Nonetheless, Superior
147 oDSGCs tended to produce more total spikes than Inferior oDSGCs in response to the drifting
148 bar stimulus (**Fig 2f**), and the total areas of their tuning curves were greater (**Fig 2g**). Similarly,
149 we noticed prominent topographic differences within cell types, with MTN-projecting RGCs in
150 ventral retina spiking more than those in dorsal retina. The firing rates of Superior and Inferior
151 oDSGCs covaried across the retina, however, and Superior oDSGCs tended to spike more than
152 Inferior oDSGCs in every retinal quadrant (**Fig S2**).

153 We wondered if the difference in response magnitude between Superior and Inferior
154 oDSGCs could be explained by a simple scaling difference of their tuning curves (i.e., same
155 shape, different size), or if it was instead associated with an asymmetry in tuning curve shape. To
156 answer this question, we first normalized the tuning curve of each cell in our data set to the
157 magnitude of its response in the preferred direction, and then rotated it such that the preferred
158 direction of each cell was aligned (**Fig 2h**). If the tuning curves of Superior oDSGCs were simply
159 scaled versions of those of Inferior oDSGCs, then this normalization and alignment procedure

160 should eliminate any apparent differences between cell types. Instead, however, we found that
161 the normalized tuning curves of Superior oDSGCs had greater widths at 50% response magnitude
162 (**Fig 2i**) and total areas (**Fig 2j**), indicating that their tuning curves were broader than those of
163 Inferior oDSGCs. In agreement, circular Gaussian fits (see Methods) of Superior oDSGC tuning
164 curves were consistently wider than those of Inferior oDSGCs (**Fig 2k**). To understand how this
165 difference in tuning curve width might affect the ability of Superior and Inferior oDSGCs to encode
166 motion, we quantified the direction selectivity index (DSI) of each cell (magnitude of the vector
167 sum divided by the scalar sum, see Methods). In agreement, the DSIs of Superior oDSGCs were
168 lower than those of Inferior oDSGCs (**Fig 2l**). Finally, we tested if these asymmetries persisted
169 across stimulus conditions by using a drifting bar stimulus with 5-fold lower contrast. As before,
170 Superior oDSGCs spiked more, had broader tuning curves, and were less direction-selective
171 compared to Inferior oDSGCs in response to the low contrast bar (**Fig 2g, j, l insets**).
172 Together, these data indicate that asymmetries in vertical OKR are concomitant with
173 prominent physiological asymmetries between Superior and Inferior oDSGCs: Superior oDSGCs
174 not only produce more total spikes than Inferior oDSGCs, but also have broader tuning curves
175 and are less direction-selective. Further, tuning curve size (i.e., area of the unnormalized tuning
176 curve) and width (i.e., area of the normalized tuning curve) were positively correlated on a cell-
177 by-cell basis (**Fig 2m**), indicating that asymmetries in these metrics could arise from a common
178 mechanism.
179
180 **Superior oDSGCs receive more excitatory input than Inferior oDSGCs**
181
182 We sought to determine the source of tuning curve asymmetries between Superior and
183 Inferior oDSGCs. As in the other primary class of direction-selective retinal ganglion cell, the ON-
184 OFF DSGCs (ooDSGCs)[40–43], oDSGCs inherit the bulk of their direction selectivity via greater
185 inhibition from starburst amacrine cells (SACs) in response to null direction stimuli[44–46] (reviewed

186 by refs. [27,47,48]). Therefore, we postulated that the difference in spike tuning curve width between
187 Superior and Inferior oDSGCs may be the result of asymmetric inhibitory inputs between the two
188 cell types.

189 To investigate this possibility, we made whole-cell voltage-clamp recordings at the
190 reversal potential for excitation to isolate inhibitory inputs to Superior and Inferior oDSGCs in
191 response to the drifting bar stimulus (**Fig 3a-b**). Across cells, we found no significant difference
192 in the magnitude of inhibitory postsynaptic currents (IPSCs) between Superior and Inferior
193 oDSGCs (**Fig 3c-d**). IPSCs to Superior oDSGCs, however, were slightly more direction-selective
194 than those to Inferior oDSGCs (**Fig 3e**). Alone, sharper IPSC direction tuning in Superior oDSGCs
195 implies sharper spike tuning curves. Our cell-attached data directly contradict this prediction (**Fig**
196 **2**). Thus, asymmetries between Superior and Inferior oDSGC spike tuning curves cannot be
197 explained by the canonical model of retinal direction selectivity involving inhibition.

198 Since inhibitory inputs failed to account for the differences between Superior and Inferior
199 oDSGCs, we wondered whether excitatory inputs could better explain the asymmetries in their
200 spike tuning curves. To test this possibility, we made voltage-clamp recordings at the reversal
201 potential for inhibition to isolate excitatory postsynaptic currents (EPSCs) during the drifting bar
202 stimulus. For every direction of stimulus motion, Superior oDSGCs had larger EPSCs than Inferior
203 oDSGCs (**Fig 3f-i**). EPSCs to Superior cells were also less direction-selective than those to
204 Inferior oDSGCs (**Fig 3j**). In agreement, the ratio of the peak EPSC to the peak IPSC (E/I) was
205 greater for Superior oDSGCs than for Inferior oDSGCs (**Fig 3k, S3**), though not different in
206 direction-selectivity (**Fig 3l)**. In addition to examining the magnitude of inputs, we also found no
207 difference in the relative timing of peak EPSCs and IPSCs across cell types (not shown). Based
208 on these results, the difference in spike tuning curve size and shape between Superior and Inferior
209 oDSGCs may be related to a corresponding shift in the balance of E/I, due in particular to an
210 asymmetry in the amount of net excitation that each cell type receives.

211 To test whether this difference in the magnitude of excitatory input to Superior and Inferior
212 oDSGCs generalized across stimulus types, we measured the spike responses and membrane
213 currents of both cell types in response to a full-field light increment (**Fig S4**). As with the drifting
214 bar, the light increment elicited more total spikes in Superior than in Inferior oDSGCs (**Fig S4f-h**).
215 We also observed a positive correlation between the magnitude of a cell's increment response
216 and the area of both its tuning curve (Sup: R^2=0.75, p=1.57x10^{-21}; Inf: R^2=0.73, p=2.13x10^{-26}) and
217 normalized tuning curve (Sup: R^2=0.23, p=0.013; Inf: R^2=0.47, p=1.18x10^{-9}). Under voltage-clamp
218 conditions, Superior oDSGCs had greater peak EPSCs and excitatory charge transfers than
219 Inferior oDSGCs in response to the increment (**Fig S4m-o**). However, there was no difference in
220 the peak IPSCs or inhibitory charge transfers between cell types (**Fig S4i-k**). Further, we found a
221 strong correlation between the maximum firing rate of a cell to the increment and the magnitude
222 of its EPSC, but not IPSC (**Fig S4l, p**). These results demonstrate that Superior oDSGCs generate
223 more spikes than Inferior oDSGCs across multiple stimuli, and, further, that this increased spike
224 output is consistently associated with differences in the amount of excitatory, but not inhibitory,
225 input.
226
227 **Postsynaptic differences may account for shifts in E/I**
228
229 Differences in the postsynaptic currents of Superior and Inferior oDSGCs could result from
230 asymmetries in presynaptic wiring and/or the postsynaptic properties of each oDSGC type. Serial
231 block-face electron microscopy[40,49,50] and analysis of dendritic stratification[21] have not yet
232 provided evidence of presynaptic wiring differences between oDSGCs with different preferred
233 directions. Thus, we investigated possible postsynaptic asymmetries that might account for the
234 differences in how Superior and Inferior oDSGCs encode motion.
235 We first analyzed the morphological features of Superior and Inferior oDSGCs by filling
236 cells of both types with dye (**Fig 4a**). Convex hull analysis revealed that the dendritic fields of

237 Superior oDSGCs covered a larger total area than those of Inferior oDSGCs (**Fig 4b**). Sholl
238 analysis, however, showed similar dendritic complexity between cell types (**Fig 4c**). To explore
239 whether synaptic differences exist between cell types, we stained for the excitatory postsynaptic
240 density scaffolding protein PSD-95[51] (**Fig 4d-g**) and the inhibitory postsynaptic scaffolding protein
241 gephyrin[52,53] (**Fig 4h-k**). These assays revealed no difference in the number or density of synaptic
242 puncta between cell types. However, Superior oDSGCs had significantly larger excitatory, but not
243 inhibitory, puncta (**Fig 4g, k**). This finding is consistent with greater amounts of excitatory input to
244 Superior oDSGCs.

245 To complement these morphological differences, electrophysiological recordings also
246 revealed a number of intrinsic differences between Superior and Inferior oDSGCs. First, the
247 membrane capacitances of Superior oDSGCs were greater than those of Inferior oDSGCs (pF,
248 Sup: 76.84±7.41; Inf: 52.47±4.59; p=0.001). Sequentially recording both the spike output and
249 EPSCs of individual oDSGCs to the full-field increment stimulus also revealed that Superior
250 oDSGCs had lower spike-to-EPSC ratios (**Fig S4p**). This observation also tended to be true for
251 each direction of the drifting bar stimulus (**Fig S3d-aa**). In agreement, the input resistances of
252 Superior oDSGCs were lower than those of Inferior oDSGCs (GOhms, Sup: 0.181±0.021; Inf:
253 0.319±0.033; p=0.004). These phenomena are each consistent with the larger size of Superior
254 oDSGCs relative to Inferior oDSGCs. We found no significant differences in other intrinsic
255 properties including the resting membrane potential (mV, Sup: -54.6±1.1; Inf: -54.7±1.5; p=0.86)
256 and spike threshold (mV, Sup: -43.7±1.17; Inf: -45.0±1.8; p=0.70). Together, these data indicate
257 that Superior oDSGCs are less intrinsically excitable than Inferior oDSGCs, but that this
258 asymmetry is outweighed by counteracting discrepancies in the magnitude of excitatory input to
259 each cell type.

260

261

262

263 **Untuned excitation broadens spike tuning curves**

264

265 That Superior oDSGCs receive relatively more excitation than Inferior oDSGCs explains
266 their greater spike output (**Fig 2f-g; S4**). Less obvious, however, is whether this difference in
267 excitatory input can also account for the wider tuning curves of Superior oDSGCs (**Fig 2h-l**). A
268 debate remains over whether excitatory inputs to DSGCs are directionally tuned[48,50,54–58]
269 (reviewed by ref. [27]). While our results indicate that MTN-projecting RGCs might receive different
270 amounts of excitation based on stimulus direction (**Fig 3j**), the majority of directionally tuned
271 inputs were inhibitory (**Fig 3m**). Further, the apparent direction selectivity of EPSCs is likely
272 partially attributable to imprecise space clamp[48,56] (but see ref. [55]). Thus, the extent to which the
273 tuning curves of Superior and Inferior oDSGCs are shaped by directionally asymmetric excitation
274 is unclear, and we remain agnostic on this point. Instead, we focus on the more pronounced
275 observation that Superior oDSGCs receive greater excitation than Inferior oDSGCs across
276 stimulus directions (**Fig 3h-i, k, S3**), regardless of the extent to which this excitation is tuned. In
277 the following experiments, we investigate the relationship between spike tuning curve shape and
278 the overall amount of excitation to an oDSGC. We ask whether and how different magnitudes of
279 excitatory input to Superior and Inferior oDSGCs can explain their difference in tuning curve width.

280 To test how the magnitude of excitation, even when directionally untuned, to an oDSGC
281 changes the shape of its tuning curve, we measured the spikes of Superior and Inferior oDSGCs
282 in current-clamp (**Fig 5a-b, h**) while injecting constant amounts of either positive (to add ~6mV,
283 "depolarizing") or negative (to subtract ~6mV, "hyperpolarizing") current across stimulus
284 directions. Importantly, the depolarizing current injections were small enough such that every cell
285 in our dataset retained a baseline firing rate of 0hz. This approach allowed us to investigate how
286 providing a cell with more or less directionally-untuned excitation influences the shape of its spike
287 tuning curve. Indeed, we found that tuning curves measured under depolarizing conditions were
288 not only larger (**Fig 5i**), but also wider than those measured under hyperpolarizing conditions on

289 a cell-by-cell basis (**Fig 5a-d, j**). In agreement, both Superior and Inferior oDSGCs were less
290 direction-selective under depolarizing relative to hyperpolarizing conditions (**Fig 5k**). Together,
291 these data demonstrate that increasing the amount of excitation to an oDSGC broadens its tuning
292 curve.

293 Interestingly, comparing these results to those recorded extracellularly in cell-attached
294 recordings revealed an additional nuance. Depolarizing current injections widened only the tuning
295 curves of Inferior oDSGCs (**Fig 5c-d, top rows of 5e-f**). In contrast, hyperpolarizing injections
296 sharpened the tuning curves of both cell types (**Fig 5c-d, bottom rows of 5e-f**). One possible
297 explanation is that while excitation generally broadens tuning curve width, greater excitatory input
298 minimally affects Superior oDSGCs (**Fig 5c**) because they are already positioned closer to an
299 upper limit on this phenomenon. Nonetheless, our results highlight a causal relationship between
300 tuning curve width and the amount of untuned excitation that an oDSGC receives.

301

302 **Spike threshold plays a dominant role in setting tuning curve width**

303

304 Two complementary mechanisms could explain how untuned excitation broadens tuning
305 curve width. In the first mechanism, excitation influences the nonlinear transformation between
306 synaptic input and spike output that is introduced by a neuron's spike threshold (**Fig 5g**). More
307 specifically, thresholding may sharpen a neuron's spike tuning curve relative to the tuning of
308 underlying membrane fluctuations by clamping spike output at zero in response to subthreshold
309 membrane responses that are likely to occur for null direction stimuli[59]. When the amount of
310 untuned excitatory input increases, however, membrane fluctuations more readily surpass the
311 spike threshold for all stimulus directions, thereby broadening the spike tuning curve. In the
312 second mechanism, untuned excitation directly circularizes the tuning curve of underlying
313 membrane potentials by increasing null direction responses proportionally more than preferred

direction responses. This “additive” contribution would then be inherited by the spike tuning curve[60].

We first tested whether thresholding effects contribute to the width of oDSGC tuning curves. To do so, we isolated the underlying subthreshold voltages (Vm) from our current-clamp recordings that also contained spikes (**Fig 5l**). Three independent observations about these Vm tuning curves each suggests that thresholding critically influences spike tuning curve width. First, unlike for spikes, depolarizing and hyperpolarizing current injections did not affect the width of Vm tuning curves (**Fig 5n-o, t-u**). The total areas of Vm tuning curves were, however, slightly larger under the hyperpolarizing condition, likely due to the marginally greater driving force on excitatory conductances in this setting (**Fig 5m**). Second, the Vm tuning curves of Superior oDSGCs were larger in magnitude than those of Inferior oDSGCs, but also narrower and more direction-selective (**Fig 5m-o arrowheads**). This result was anticipated from our voltage-clamp recordings which indicated that inhibition is more direction-selective in Superior oDSGCs (**Fig 3e**). It also suggests, however, that the spike tuning curve width of oDSGCs is not directly inherited from that of the underlying membrane potentials, and instead reflects the interplay between Vm magnitude and spike threshold. Third, comparing the width of Vm tuning curves to those measured simultaneously in spikes revealed that the spike tuning curves were substantially sharper than those of the subthreshold voltages for both depolarizing and hyperpolarizing injections (**Fig 5p-s**). The difference between the shapes of the spike and Vm tuning curves was smaller for the depolarizing condition, however, because in this condition the majority of stimulus directions elicited Vm responses that eclipsed the spike threshold (**Fig 5v-w**). Together, these three results each corroborate the notion that thresholding plays a prominent role in setting spike tuning curve width relative to the amount of untuned excitation that an oDSGC receives.

To test the extent to which excitation broadens oDSGC tuning curves through additive effects, we recomputed Vm tuning curves after including a constant, additive offset that reflected the average current injection supplied during depolarizing and hyperpolarizing injections. These

340 offset-corrected Vm tuning curves were significantly wider under depolarizing conditions than they
341 were under hyperpolarizing conditions (**Fig S5**). However, the observation that (uncorrected) Vm
342 tuning curves — in which putative additive differences *between* cell types are expected to persist
343 — were more sharply tuned for Superior than Inferior oDSGCs (**Fig 5n-o arrowheads**) indicates
344 that thresholding has a greater influence on spike tuning curves than does additive excitation. In
345 agreement, current injections caused significantly larger changes in spike tuning curves than in
346 offset-corrected Vm tuning curves (**Fig 5t-u**). These results demonstrate that while untuned
347 excitation likely has some additive effect, complementary thresholding has greater influence over
348 oDSGC spike tuning curves.
349

350 **A parallel conductance model recapitulates the influence of thresholding on oDSGC**
351 **direction tuning**
352

353 Together, our current injection experiments suggest that (1) spike thresholding plays a
354 prominent role in setting the width of oDSGC tuning curves, and (2) additive effects are likely
355 present but do not dominate. To independently test these findings, we built a parallel conductance
356 model of an oDSGC based on empirically measured parameters from a separate set of cells to
357 those used for the current injection experiments. Among these parameters were 8 separate
358 inhibitory conductances for each stimulus direction, and a single, directionally-untuned excitatory
359 conductance (**Fig 6a-b**). We then tested how manipulating the gain of the excitatory conductance
360 affected tuning curves generated from either spikes or the peak subthreshold membrane
361 potentials (**Fig 6c-f**) (see Methods).
362 As in our empirical data, we found that increasing the gain of untuned excitation to the
363 model oDSGC increased the total area of both spike and Vm tuning curves (**Fig 6d**). However,
364 while the spike tuning curve rapidly widened and became less direction-selective with increasing
365 excitatory gain, the shape of the Vm tuning curve was much less dependent on excitatory gain

366 (**Fig 6e-f**). The stark difference between the spike and Vm trajectories can only be attributed to
367 thresholding effects. On the other hand, the shallow slope of the Vm curve reflects the additive
368 contribution of excitation. Consistent with our physiological results, thresholding played a critical
369 role in setting the model oDSGC's tuning curve width, whereas additive effects were relatively
370 minor. Further, the prior observation that depolarizing current injections influenced Superior
371 oDSGCs less than Inferior oDSGCs (**Fig 5c-f**) is supported by the diminishing marginal effect of
372 additional excitatory gain on spike tuning curve width. We also noticed that the average
373 empirically measured normalized tuning curve area and DSI from our cell-attached recordings
374 (**Fig 6e-f circles**) fell within the regime where these metrics were steeply dependent on excitatory
375 gain. In this regime, thresholding effects render small changes in synaptic inputs particularly
376 influential for oDSGC direction tuning.
377
378 **Thresholding effects produce contrast-sensitive direction tuning in oDSGCs**
379
380 The dependence of oDSGC tuning on thresholding predicts that any stimulus which
381 influences the magnitude of synaptic inputs may also alter tuning curve shape. We tested this
382 hypothesis by comparing the tuning curves of Superior and Inferior oDSGCs in response to high
383 contrast (stimuli used in all previous figures) and low contrast (5-fold dimmer) drifting bars. For
384 most cells, low contrast bars elicited fewer total spikes (**Fig 7a-b**). However, as for high contrast
385 stimuli, Superior oDSGCs tended to spike more and have broader tuning curves than Inferior
386 oDSGCs in response to low contrast bars (**Fig 2g, j, l, insets**). Interestingly, cells of both types
387 had sharper spike tuning curves in response to low, compared to high, contrast stimuli (**Fig 7c-**
388 **d**). To test whether this contrast-sensitivity could be attributed to thresholding effects, we
389 measured the tuning curves of subthreshold membrane potentials. While the area of Vm tuning
390 curves was greater under high contrast conditions (**Fig 7e**), Vm tuning curve width and direction
391 selectivity did not change with contrast (**Fig 7f-g**). In agreement, the fraction of spike tuning curves

392 that sharpened under low contrast was significantly different than the equivalent fraction of Vm
393 tuning curves that followed the same trend (normalized area: p=0.0019; DSI: p=0.0046; 2-sided
394 Fisher's exact) (**Fig 7c-d, f-g**), and Vm tuning curves were less affected by stimulus contrast than
395 the tuning curves of simultaneously measured spikes (**Fig 7h-i**). These results indicate that
396 thresholding is critical to setting oDSGC spike tuning curve width across stimulus contrasts, just
397 as it is across cell types.

398 Our finding that oDSGCs are contrast-sensitive departs from previous work which has
399 shown that direction tuning in ooDSGCs is contrast-invariant[61–63]. Contrast-invariance in
400 ooDSGCs appears to rely on the stability of E/I across contrasts. For this reason, we tested
401 whether the contrast-sensitivity of oDSGCs was associated with a mutable E/I by sequentially
402 measuring excitatory and inhibitory synaptic currents for preferred and null direction stimuli across
403 contrasts. Our data show that E/I in neither the preferred nor null direction changes systematically
404 with contrast (**Fig 7j-k**). Further, the fraction of spike tuning curves that sharpened under low
405 contrast conditions was significantly greater than the fraction of E/I ratios that were lower under
406 low contrast conditions (normalized area: PD p=0.0132, ND p=0.0132; DSI: PD p=0.0044, ND
407 p=0.0044; 2-sided Fisher's exact) (**Fig 7c-d, j-k**). These results suggest that as in ooDSGCs, E/I
408 in oDSGCs is relatively stable across contrasts. However, the spike tuning curves of oDSGCs are
409 nonetheless contrast-sensitive. Thus, stable E/I alone is insufficient to maintain the contrast-
410 invariance of spikes. In the case of oDSGCs, changes to the absolute magnitude of synaptic
411 inputs across contrasts, along with thresholding effects, appear to trump the contrast-invariance
412 of E/I.

413 To further test the extent to which the magnitude of synaptic inputs can affect oDSGC
414 tuning curves even with stable E/I, we revisited our parallel conductance model of an exemplary
415 oDSGC. We modeled oDSGC responses while changing the gain of excitatory and inhibitory
416 conductances together, thereby keeping E/I constant while nevertheless adjusting the total
417 magnitude of E and I. As in our empirical data, we found that lowering the gain of E and I together

418 to simulate responses to low contrast stimuli resulted in sharper spike tuning curves. The width
419 of Vm tuning curves, however, remained relatively contrast-invariant (**Fig 7I**). These results
420 recapitulate our empirical findings and indicate that the spike threshold nonlinearity influences
421 spike tuning curve width across contrasts. Other stimulus parameters that affect the magnitude
422 of excitation, inhibition, or both are also likely to modulate the direction coding properties of
423 oDSGCs.
424
425 **A subtraction algorithm predicts vertical OKR from oDSGC activity**
426
427 Having established the tuning properties of Superior and Inferior oDSGCs, we asked
428 whether the asymmetries between these cell types, along with their contrast-sensitivities, could
429 explain how vertical OKR changes across stimulus conditions. Cross-species work has
430 established that Superior and Inferior oDSGCs are likely centrally integrated by a subtraction
431 algorithm[3,22,64]. In this model, OKR is predicted on the basis of the *difference* in spike rate between
432 Superior and Inferior oDSGCs, rather than by the absolute spike rate of either cell type. A number
433 of observations support this model: (1) stimuli that activate both Superior and Inferior oDSGCs
434 [e.g. a full-field increment of light (**Fig S4**)] do not elicit OKR, (2) stimuli that differentially activate
435 Superior and Inferior oDSGCs (e.g. drifting gratings) maximally drive OKR (**Fig 1, 2**), (3) Superior
436 and Inferior oDSGCs project to separate MTN subnuclei[21,22] that are mutually connected by
437 inhibitory interneurons (i.e., a simple differentiating circuit)[22,65], (4) MTN neurons prefer either
438 superior or inferior motion[21,22,64,66–68], but their preferred and null directions are not 180° apart;
439 instead, they correspond to the preferred directions of opposing oDSGC types[64,67,68], which may
440 differ by less than 180° [15] (but see ref. [16]), and (5) MTN neurons maintain moderate baseline spike
441 rates that are not only augmented by preferred direction stimuli, but also diminished by null
442 direction stimuli[64,66–68]. Together, along with the simplicity of the vertical OKR pathway and its
443 isolation from other visual circuits, these lines of evidence all point to a circuit motif in which MTN

444 neurons encode the difference in spike rate between Superior and Inferior oDSGCs. Thus,
445 superior OKR likely occurs when Superior oDSGCs spike significantly more than Inferior
446 oDSGCs, and vice versa. The robustness of OKR is putatively related to the magnitude of the
447 spike rate difference (**Fig 8a**).

448 We used our empirically recorded electrophysiology data from Superior and Inferior
449 oDSGCs to generate hypotheses for how OKR gain would change across stimulus conditions
450 (**Fig 8b**). To do so, distributions of Superior and Inferior oDSGC firing rates were compared for
451 superior and inferior drifting bars at high and low contrast (i.e., four stimulus conditions) (**Fig 8c-**
452 **f**). We inferred that the relative gain under each stimulus condition would be related to the
453 corresponding difference in spike rate between Superior and Inferior oDSGCs under that same
454 condition. For instance, gain in response to a high contrast superior grating was predicted by the
455 difference between the preferred direction responses of Superior oDSGCs and the null direction
456 responses of Inferior oDSGCs to high contrast bars. Behavioral predictions about how gain would
457 change across stimulus conditions were made by comparing bootstrapped distributions of such
458 differences (**Fig 8g-h, k-l**). Importantly, these inferences constitute linear predictions of gain.
459 Allowing for the possibility that downstream circuitry incorporates additional monotonic
460 nonlinearities, a linear prediction is consistent with behavior so long as it predicts gain changes
461 in the correct *direction* (but not magnitude) across stimulus conditions.

462 The asymmetries in the tuning curves of Superior and Inferior oDSGCs resulted in four
463 first-order predictions for how OKR gain changes across stimulus conditions: (1) for superior
464 stimuli, gain is greater in response to high contrast stimuli than to low contrast stimuli (**Fig 8g**),
465 (2) for inferior stimuli, gain is greater in response to high contrast stimuli than to low contrast
466 stimuli (**Fig 8h**), (3) at high contrast, gain is greater in response to superior stimuli than to inferior
467 stimuli (**Fig 8k**), and (4) at low contrast, gain is greater in response to superior stimuli than to
468 inferior stimuli (**Fig 8l**). We also generated two additional second-order hypotheses that rely on
469 an approximately linear relationship between differences in oDSGC output and gain in the tested

470 regime: (5) gain is higher under high contrast, regardless of stimulus direction (**Fig 8o, s**), and (6)
471 behavioral asymmetries in response to superior and inferior stimuli diminish with decreasing
472 contrast (**Fig 8p, s**). Thus, our physiological data generate clear predictions for how the tuning
473 properties of oDSGCs affect OKR across stimulus conditions.

474 We next tested these predictions in behaving mice. OKR in the superior and inferior
475 directions was measured in response to high and low contrast oscillating gratings. Our results
476 revealed that all six of our linear predictions were consistent with behavior (**Fig 8i-j, m-n, q-r, u,**
477 **S6**). Most notably, gain decreased with contrast (**Fig 8q, u**), and the asymmetry between superior
478 and inferior OKR that we originally noticed under high contrast conditions diminished in response
479 to low contrast stimuli (**Fig 8r, u**). This latter observation is consistent with our linear prediction
480 that the net change in eye position over the course of a single oscillation would be greater for high
481 contrast stimuli (**Fig 8p, s**). While this result may be related to the overall decrease in gain under
482 low contrast, it is certainly not *necessitated* by that phenomenon and relies on further subtleties
483 in the relationship between Superior and Inferior oDSGC responses at both contrasts. Indeed,
484 permuting the behavioral predictions by scrambling which cellular responses were assigned to
485 superior/inferior motion and high/low contrast revealed that only 5 permutations (out of 256
486 possibilities, 1.95%) accurately matched our behavioral results. Consistent with these findings,
487 the relationship between our cellular linear predictions and behavioral results were fit well by a
488 simple monotonic function that was approximately linear within the measured regime (**Fig 8t**).
489 Taken together, these results provide a neurophysiological explanation for how vertical OKR
490 changes across multiple stimulus conditions and reveal that the circuit and cellular properties that
491 shape oDSGC tuning curves have direct and predictable consequences for behavior.
492
493
494
495

496 **DISCUSSION**

497

498 Our results depict a neurophysiological mechanism by which vertical OKR changes across
499 stimulus conditions. We demonstrate that superior and inferior OKR are asymmetric in adult mice
500 (**Fig 1**), and show how this behavioral phenomenon can be traced to novel asymmetries in the
501 direction tuning properties of Superior and Inferior oDSGCs (**Fig 2**). Mechanistically, a shift in the
502 balance of excitatory and inhibitory inputs across cell types influences direction tuning, primarily
503 through an effect associated with spike thresholding (**Fig 3-6**). Similar thresholding effects also
504 confer contrast-sensitivity of the spike tuning curve, even when E/I is contrast-invariant (**Fig 7**).
505 Together, these cellular properties accurately predict how vertical OKR changes in response to
506 stimulus direction and contrast (**Fig 8**).

507 Directional asymmetries in OKR are common across species. Besides the vertical
508 asymmetries that we investigated here, horizontal OKR is asymmetric in many organisms[2,69]. This
509 asymmetry manifests nearly universally as higher OKR gain in response to temporal-to-nasal
510 (anterior) motion than to nasal-to-temporal (posterior) motion, and often only when stimuli are
511 viewed monocularly. It is tempting to speculate that these horizontal asymmetries may similarly
512 be linked to direction tuning in the retina. While anterior-preferring oDSGCs are critical to
513 horizontal OKR[12,24,39], posterior-preferring oDSGCs were only recently identified in rodents and
514 display definitively weaker direction tuning properties than their anterior-preferring counterparts[16].
515 Further, a subtraction mechanism between horizontally tuned oDSGCs may also underlie
516 horizontal OKR[33]. However, at least two confounds obscure a connection between the tuning
517 properties of Anterior and Posterior oDSGCs and asymmetries in horizontal OKR. First, oDSGCs
518 in the left and right eyes, and their contralateral central targets (NOT/DTN), encode different
519 absolute directions of stimulus motion (reflection occurs over the sagittal body axis). To
520 compensate, signals are compared across eyes/hemispheres prior to behavior[33], and, in some
521 species, NOT/DTN receives descending, often binocular, inputs from visual cortex[2,13,70,71].

522 Second, recent studies have suggested that ooDSGCs could be involved in horizontal OKR[17,23].
523 Asymmetries in the horizontal version of the behavior may thus depend on more complex
524 considerations.

525 Analogous confounds are less concerning when considering the mechanisms that could
526 account for asymmetries in vertical OKR. For one, stimuli that induce vertical OKR, such as the
527 gratings used here, are perceived identically by both eyes. Interhemispheric communication is
528 unlikely to influence behavior under such conditions. Though signals are probably also exchanged
529 between the horizontal and vertical OKR pathways[3,13,18], these channels likely play a minimal role
530 in shaping OKR to purely vertical stimuli[33]. Finally, while it has been suggested that a vertically-
531 tuned ooDSGC may also project to MTN[23], this cell type was not clearly revealed by either
532 anatomical or electrophysiological analyses during our retrograde labeling experiments (**Fig S1,**
533 **S4**). Instead, we find that two populations of ganglion cells project to MTN, and that these cells
534 can be classified as Superior and Inferior oDSGCs (**Fig S1**). These results are consistent with
535 characterizations of MTN-projecting RGCs across many species[20,21,72–74]. Thus, unlike for
536 horizontal OKR, asymmetries in vertical OKR can be explained more simply by the physiology of
537 oDSGCs.

538 Despite the possibility that asymmetries in vertical and horizontal OKR are influenced by
539 separate mechanisms, the two phenomena could share a common ethological function. Optic
540 flow associated with forward locomotion typically includes a large posterior component. Thus, it
541 has been suggested that posterior OKR is less reliable than anterior OKR in order to mitigate
542 lateral eye movements that might otherwise occur when an animal walks forward[75]. Similar
543 reasoning may explain the asymmetry between superior and inferior OKR[28,35,37]. Indeed, recent
544 work in freely moving mice demonstrated that optic flow has a stronger inferior than superior
545 component[76]. Further, optic flow was largest in dorsal retina, which could explain our additional
546 observation that stronger stimuli were required to activate Superior and Inferior oDSGCs alike in
547 dorsal relative to ventral retina (**Fig S2**). Thus, the cellular and behavioral asymmetries identified

548 in this study may serve to mitigate the influence of natural locomotion on OKR. Future work should
549 address this possibility by mapping OKR gain as a function of the extent to which various stimuli
550 reflect locomotion-associated optic flow.

551 From a physiological perspective, our results provide the first evidence that Superior and
552 Inferior oDSGCs encode motion asymmetrically. This finding coincides with previous work
553 demonstrating genetic and anatomical differences between oDSGC types. Multiple transgenic
554 lines are known to label either Superior or Inferior oDSGCs, but not both[18,20,21,74]. The axons of
555 Superior and Inferior oDSGCs take separate retinofugal tracts and project to different MTN
556 subnuclei in mice[21]. Additional differences exist between vertically- and horizontally-tuned
557 oDSGCs[12,24]. The competitive advantage of directionally-asymmetric OKR may have thereby
558 shaped the development of many differences between oDSGC types.

559 The asymmetric spike tuning of Superior and Inferior oDSGCs is associated with
560 differences in the magnitude of excitatory synaptic input to each cell type (**Fig 3**). Three synaptic
561 partners are primary candidates for the source of this asymmetry: (1) glutamatergic input from
562 bipolar cells (types 5 and 7), (2) cholinergic input from SACs, and (3) glutamatergic input from
563 VGluT3 amacrine cells[44–46,49,50,58,77,78]. Glutamatergic conductances in oDSGCs rely on AMPARs
564 and NMDARs, whereas cholinergic conductances rely on nicotinic AChRs[79]. These conductances
565 have been studied primarily in ooDSGCs and deserve further characterization in oDSGCs.
566 Interestingly, VGluT3 amacrine cells also corelease glycine, which cancels oDSGC spiking in
567 response to high-velocity stimuli[49,57,77,78]. Asymmetries at the VGluT3-oDSGC synapse could
568 coincide with differences in the speed tuning properties of Superior and Inferior oDSGCs. A
569 combination of genetic, optical, and pharmacological manipulations could distinguish among
570 these possible sources of asymmetric tuning.

571 Further insight into how oDSGCs encode motion can be gained by comparing their tuning
572 properties to those of the more comprehensively studied ooDSGCs. While prior work has focused
573 on speed tuning as the primary difference between oDSGCs and ooDSGCs[14,26,49,57,78], our results

574 reveal an additional difference between these two classes of DSGCs that has been previously
575 overlooked: oDSGCs are contrast-sensitive (**Fig 7**), whereas ooDSGCs are not[62]. In ooDSGCs,
576 preservation of E/I across contrasts is apparently critical for retaining contrast-invariant direction
577 tuning[61,63]. Counterintuitively, we find that E/I in oDSGCs is also relatively stable across contrasts.
578 Therefore, stability of E/I is not alone sufficient for contrast-invariant spike tuning; independence
579 from thresholding effects is also required. Indeed, thresholding modulates oDSGC direction tuning
580 following changes to either E/I (**Fig 5-6**) or the absolute magnitude of E and I (**Fig 7**). Evidently,
581 the influence of thresholding constitutes a major difference in the mechanisms that govern how
582 oDSGCs and ooDSGCs encode motion.

583 That E/I is contrast-insensitive in both oDSGCs and ooDSGCs also indicates some extent
584 of shared circuitry between these cell types. Contrast-invariance of E/I in ooDSGCs relies on
585 postsynaptic NMDA conductances and constrains possible presynaptic wiring motifs[61,63].
586 oDSGCs likely share many of these features. Indeed, serial block-face electron microscopy has
587 confirmed that oDSGCs and ooDSGCs share many of their presynaptic partners[40,43,49,50,54].
588 Nonetheless, differences in the intrinsic properties between and within DSGC classes, including
589 dependence on thresholding, could magnify the impact of subtle circuit differences on spike
590 output.

591 Finally, our results show that vertical OKR is predicted by a simple subtraction between
592 the outputs of Superior and Inferior oDSGCs (**Fig 8**). It is interesting that asymmetries in oDSGCs
593 are not apparently corrected by downstream circuitry, considering that normalization operations
594 pervade the nervous system[80]. One explanation is that there is no simple compensatory solution
595 to normalize the responses of Superior and Inferior oDSGCs because multiple stimulus
596 parameters (e.g., stimulus direction and contrast) simultaneously affect the asymmetry
597 magnitude. On the other hand, the ethological advantage of asymmetric OKR may have provided
598 sufficient evolutionary pressure to allow asymmetries between Superior and Inferior oDSGCs to
599 propagate to behavior when they might otherwise have been compensated. Regardless, a linear

600 subtraction of oDSGC outputs offers an accurate and parsimonious explanation of vertical OKR.
601 Moreover, this algorithm fits well with both the anatomy and physiology of MTN and the isolation
602 of the vertical OKR pathway from other visual circuits[13,21,22,64–68].

603 Similar subtraction algorithms are prevalent across the animal kingdom. In the mammalian
604 retina, such a computation confers both the spatial center-surround[81–83] and chromatic
605 dichotomy[84–86] of receptive fields. In Drosophila, spatially offset antennae allow accurate
606 estimation of wind velocity by differentiation of signals across two input sites[87]. Similar
607 mechanisms likely underlie tropotaxic orienting behaviors that also rely on spatially offset
608 receptors, including arthropod antennae[88], reptile forked tongues[89], and mammalian ears[90]. The
609 ubiquity of this circuit motif may reflect an efficient solution for integrating complementary
610 information streams. Our results highlight how such circuits can be influenced by subtle
611 asymmetries across input channels. Further investigation will determine whether diverse sensory
612 systems rely on asymmetric inputs to adaptively change behavior across stimulus conditions.

613

614

615 **METHODS**

616

617 **Statistics:** All metrics reported in the text refer to population mean±SEM unless otherwise
618 specified. Nonparametric hypothesis tests were used to compute significance values wherever
619 possible. Mann-Whitney U tests were used for instances in which the test type is not specified.
620 Wilcoxon signed-rank and Fisher's exact tests were used where specified in the text and/or figure
621 legends. All tests were two-sided. R^2 values are Pearson correlation coefficients. Significance
622 markings are as follows: not significant (N.S.) $p \geq 0.05$, *$p<0.05$, **$p<0.01$, ***$p<0.001$.

623

624 **Animals:** Adult wildtype C57BL/6 mice between the ages of postnatal day P60 and P100 of both
625 sexes were used for all experiments. Animals were kept on a 12 hour dark-12 hour light cycle with

626 continuous access to food and water. All experiments were performed in accordance with
627 protocols approved by the University of California, San Francisco Institutional Animal Care and
628 Use Program.
629
630 **Behavior rig**: To accurately evoke and measure OKR, we custom designed a behavior rig that
631 was capable of presenting full-field, binocular stimuli to behaving mice. The design of the rig was
632 based on Denman et al., 2017[38]. Briefly, an acrylic hemisphere (diameter=24", California Quality
633 Plastics) was covered with a custom paint that had 50% diffuse reflectivity between 350 and
634 750nm (Twilight Labs) in order to limit reflections within the hemisphere. Stimuli were emitted
635 from a DLP projector with peak emission at 405nm (LightCrafter through EKB Technologies) and
636 were reflected onto the hemisphere via a silver-coated brass hemisphere ("convex mirror",
637 diameter=6", Wagner). Stimuli were built using Psychopy (www.psychopy.org) and a custom
638 wrapper to manage their sequential presentation and alignment with eye tracking videos. The
639 wrapper and stimuli are both available at https://github.com/ScottHarris17/Bassoon. Aberrations
640 in the projection were corrected by applying a manually-fit spherical morph to all stimuli
641 (Meshmapper, www.paulbourke.net). Blackout curtains surrounded the rig to minimize light
642 contamination.
643
644 **Unidirectional OKR stimuli:** Unidirectional sinusoidal gratings were presented in groups of 6
645 consecutive epochs. Each epoch consisted of 20s of a static grating, followed by 60s of a grating
646 drifting either directly upward or directly downward, and an additional 20s of a static grating. The
647 6 total epochs consisted of 3 upward and 3 downward epochs that were randomly interleaved. All
648 gratings moved at 10°/s and had a spatial frequency of 0.15 cycles/°. The brightest part of the
649 grating evoked 1.38×10^3 S-cone photoisomerizations/s and the darkest part of the grating evoked
650 25.9 S-cone photoisomerizations/s. M-cone photoisomerizations were 60% those of S-cone.
651

652 **Oscillating OKR stimuli:** Oscillating sinusoidal gratings were presented in groups of 3
653 consecutive epochs. Each epoch consisted of 20s of a static grating, followed by 120s of
654 oscillation, and an additional 20s of a static grating. During the oscillation, the grating velocity was
655 modulated sinusoidally up and down. The oscillation had an amplitude of 20°, a period of 15s,
656 and a phase shift of 0°. 8 oscillations were completed over the course of one epoch. All gratings
657 had a spatial frequency of 0.15 cycles/°. The intensities of high contrast oscillating gratings were
658 equivalent to those used for unidirectional OKR stimuli and had 5-fold greater Michelson contrast
659 than low contrast oscillating gratings. High and low contrast gratings had the same mean
660 luminance.
661
662 **Eye tracking:** Prior to eye tracking experiments, animals underwent stereotaxic surgery for
663 implantation of a custom head-fixing apparatus. After surgery, animals were given 7 days to
664 recover. Animals were then gradually habituated to the behavior rig by spending increasing
665 amounts of time head-fixed on the rig for five consecutive days prior to the beginning of
666 experiments.
667 Eye tracking experiments were run over the course of up to 3 days per animal. Each
668 animal spent no more than 30 minutes per day on the rig. During experiments, mice were head-
669 fixed in the center of the hemisphere, which filled the entirety of their visual field. Eye movements
670 were recorded using a GigE camera (Photonfocus), an infrared filter, and a hot mirror (Edmund
671 Optics) that allowed the camera to be positioned outside of the animal's field of view. Infrared
672 LEDs (880nm) were mounted on the top and side of the camera to generate corneal reflections
673 that marked the meridian and equator of the eye, respectively. StreamPix software (NorPix) was
674 used to capture video of the eye and align it to stimuli via TTL signals.
675 After completion of the experiments, Deeplabcut (www.deeplabcut.org) was used to train
676 a neural network to locate the pupil and corneal reflection on each video frame. The two
677 dimensional pupil location was then translated to angular eye position for every recording frame

using the methods described by Stahl et al., 2000, 2004[91,92] and Zoccolan et al., 2010[93]. In short, prior to experiments, we calibrated the eye tracking system for each animal by repeatedly swinging the camera ±6° in the horizontal plane and measuring the relative position of the pupil and corneal reflection. This process was repeated across 5 different luminances to fit a linear regression between pupil size and angular eye position. The meridian and equator of the eye were measured by turning on the top- and side-aligned infrared LEDs in sequence. During experiments, only the top LED was on. Angular eye position was then calculated as $\phi = arcsin(\frac{\Delta x}{\sqrt{R_{p0}^2 - \Delta y^2}})$ [Eq. 1] and $\theta = arcsin(\frac{\Delta y}{R_{p0}})$ [Eq. 2], where ϕ is the horizontal eye position, θ is the vertical eye position, Δx is the horizontal distance measured between the eye center and the pupil, Δy is the vertical distance measured between the eye center and the pupil, and R_{p0} is the radius of rotation between the pupil and the eye's center, which was computed empirically for each pupil diameter for each animal. For all stimuli, fast and slow phases of nystagmus were separated on the basis of eye velocity and acceleration using custom MATLAB scripts. For all analyses in this report, we consider only θ, the vertical eye position, and $\Delta\theta/\Delta t$, the vertical component of eye velocity.

By measuring the vertical eye velocity ($\Delta\theta/\Delta t$) in response to the static gratings (multiple contrasts) that occurred before the onset of all stimuli, we also computed a baseline median eye drift of 0.0787°/s (IQR: 4.1792°/s; p=0.015) in the ventral direction across animals. This drift may reflect either the error associated with the estimation of the eye's center during our calibration process, or a natural biological eye drift associated with our rig. It is not possible to disambiguate between these possibilities. Since the eye position was near neutral for the time in which this drift was calculated, we baseline subtracted it from the eye position traces for all oscillating grating stimuli (for which the average eye position was also approximately neutral). For unidirectional gratings, we were unable to calculate an appropriate drift for baseline subtraction since the eye position was not often near neutral during these stimuli (**Fig S6**).

703

704 **Retrograde labeling:** MTN-projecting retinal ganglion cells were labeled via stereotaxic injection
705 of red fluorescent retrobeads (Lumafluor) into MTN. Prior to surgery, mice were anesthetized by
706 IP injection of ketamine/xylazine and 5% isoflurane inhalation. Once fully anesthetized, as
707 assessed by absence of the pedal reflex, animals were transferred to a sterile heated surface and
708 the eyes were covered with a lubricating ointment. 2% isoflurane was administered continuously
709 to maintain anesthesia. Fur was removed prior to incision and lidocaine (<7mg/kg) was injected
710 locally under the scalp. After incision, animals' heads were leveled by aligning bregma and
711 lambda in the horizontal plane. A burr hole was drilled at A/P: 0.00mm, M/L: 0.85mm from bregma.
712 All injections were performed into the right MTN. A glass needle filled with retrobeads (diluted 1:3
713 in di-water) and connected to a Hamilton syringe was lowered into the burr hole at an angle of
714 30° A/P to a depth of 5.36mm below the surface of the brain. After 10 minutes, an injection of
715 400nL was made at a rate of 5nL/s. After injection, the needle was left in place for an additional
716 10 minutes before removal. The scalp was sutured and animals recovered in a heated cage.
717 Analgesics [buprenorphine (0.05-0.1mg/kg) and NSAIDs (5-10mg/kg)] were delivered via
718 subcutaneous injection immediately after animals awoke from anesthesia, again 12 hours later,
719 and a third time the following morning. Animal health was monitored for three days after surgery
720 and additional analgesics were administered as required. Labeling of retinal ganglion cells in the
721 contralateral eye was typically observed as soon as 48 hours following surgery and did not
722 increase with time.

723

724 **Empirical mosaic analysis:** All mosaic analyses occurred ≥2 days after injection of the
725 retrograde tracer into MTN. Retinas were dissected, fixed in 4% PFA for 20 minutes, and flat-
726 mounted onto a microscope slide with a spacer. One widefield fluorescent image was taken of
727 each retina. The location of each labeled cell in the image was determined using custom MATLAB
728 scripts. Only retinas with near complete labeling (determined as greater than 500 identified RGCs)

729 were included in analyses. The retina perimeter, optic nerve head, and dorsal-ventral axis were
730 manually measured. These points were used to define a normalized polar coordinate system that
731 allowed for the comparison of cell locations and densities across retinas. Density recovery profiles
732 were calculated using the methods described by Rodieck, 1991[94].
733
734 **Mosaic models:** To model spatial distributions of single and multiple mosaics, we randomly
735 generated mosaics in a model circular retina that had an equivalent radius to that of the average
736 whole-mount retina used for empirical density recovery profile estimation. "Cell bodies" were
737 modeled as circles with radius 15μm and scattered randomly across the model retina so long as
738 the following conditions were met: (1) No two cell bodies can overlap in space (i.e., cells must
739 form a 'monolayer'), and (2) Adjacent cells that are members of the same mosaic must obey a
740 (noisy) exclusion zone that is set by the mosaic coverage factor (number of cells/retina area).
741 Coverage factors were changed systematically such that the total number of cells across all
742 mosaics - regardless of the number of mosaics being modeled - always approximated the number
743 of retrogradely labeled cells per retina in our empirical data set. Density recovery profiles were
744 computed as described for empirical data.
745
746 **Electrophysiology tissue preparation:** All electrophysiology experiments occurred ≥2 days
747 after injection of the retrograde tracer into MTN. Prior to electrophysiology experiments, mice
748 were dark-adapted for ≥12 hours. Mice were then euthanized via cervical dislocation and the left
749 eye was enucleated (contralateral to the right MTN injection). Retina dissections occurred in the
750 dark using infrared converters and warmed bicarbonate-based Ames solution, equilibrated with
751 95% O_2/5% CO_2. Brains were simultaneously harvested and fixed in 4% PFA for imaging and to
752 confirm that the retrograde tracer was properly injected into MTN. Retinas were whole mounted,
753 keeping track of orientation, and continuously perfused at 10mL/min with freshly equilibrated
754 Ames heated to 35°C throughout the course of experiments.

755

756 **Retinal location of recorded cells:** At the beginning of electrophysiology experiments, the
757 center and radius of the retina were measured: two-dimensional coordinates of 8 standardized
758 points around the perimeter of the retina were noted. The center of the retina was estimated by
759 computing the median of the circumcenters of all unique triangles that could be formed from these
760 8 points. The radius of the retina was estimated by finding the median radius of the circles that
761 circumscribed these same triangles. In all cases, the convex hull of the whole-mount retina was
762 well approximated by a circle and the retina center estimation was near the optic nerve head. The
763 coordinates of each recorded cell were computed in reference to the retina center. Cell locations
764 were combined across retinas by normalizing to the estimated radius in a polar coordinate system.
765

766 **Identification of MTN-projecting RGCs:** An NIR light source (950nm, Sutter) was used to
767 visualize the tissue for the majority of the experiment. To identify retrogradely-labeled ganglion
768 cells, a green epifluorescent light was turned on briefly (~1-3s) prior to recording from each cell.
769 This light evoked a moderate number of spikes in oDSGCs, but did not compromise their
770 responses to other stimuli. At least 1 minute of darkness was provided between the offset of the
771 epifluorescent light and the beginning of subsequent experiments.
772

773 **Electrophysiology:** Patch electrodes were pulled from borosilicate glass (Sutter) to 3-5MOhm
774 resistance using a Narishige puller. A MultiClamp 700B Amplifier (Axon Instruments) was used
775 for all recordings. Cell-attached experiments were performed using electrodes filled with HEPES
776 buffered Ames. Voltage-clamp experiments were performed using fresh electrodes filled with
777 cesium methane sulfonate[95]. Current-clamp experiments were performed using fresh electrodes
778 filled with potassium aspartate[96]. A subset of cells were recorded in both cell-attached and whole-
779 cell configurations. In these cases, cell-attached recordings were performed first. Voltage-clamp
780 and current-clamp recordings were never made from the same cell. Electrophysiology

781 experiments were conducted using Symphony DAS (https://symphony-das.github.io/) and light
782 stimuli were constructed and presented using Stage (https://stage-vss.github.io/).
783
784 **Light increment stimulus:** Light increments were the first stimulus to be presented, and were
785 often additionally interleaved between other stimuli. Light increments were delivered from an LED
786 with peak emission at 405nm from darkness for 1s, and had an intensity of 8.6×10^4 S-cone
787 photoisomerizations/s. M-cone photoisomerizations were 79% those of S-cone. The LED spot
788 had diameter 500μm or 300μm (no significant difference was observed in the responses to either
789 spot size), was centered on the cell body of each recorded cell, and was focused on the
790 photoreceptor layer of the retina.
791
792 **Drifting bar stimulus:** Drifting bars were presented from a DLP projector with peak at 405nm
793 (LightCrafter through EKB Technologies, same model as used for behavioral experiments). The
794 native optics of the projector were replaced with neutral density filters and optics to focus stimuli
795 on the photoreceptor layer of the retina via a condenser. The projector covered a rectangular area
796 of 427x311μm which was centered on the soma of each recorded cell. Drifting bars had a width
797 of 3.2° and moved at 10°/s using a conversion factor of 31μm/° [97]. Bar height was limited only by
798 the area covered by the projector. High contrast bars measured 2.4×10^4 S-Cone
799 photoisomerizations/s and were presented on top of a background of 124 S-cone
800 photoisomerizations/s. M-cone photoisomerizations were 74% those of S-cone. See below for the
801 specifications of low contrast bars. For tuning curve estimation, bars moved in 8 directions
802 separated by 45°. The presented sequence of stimulus directions was randomized for each
803 recording. Tuning curves were estimated by mean measurements taken over 5 repetitions per
804 stimulus direction.
805

Tuning curve area: Tuning curve area was calculated by dividing the area under the curve of the linear tuning curve by 360°. For clarity, this metric is also referred to as the "linear tuning curve area."

Preferred direction: The preferred direction was calculated as the direction of the vector sum of responses to all 8 stimulus directions. Thus, the preferred direction was not necessarily equivalent to the single stimulus direction that evoked the largest response. The null direction was defined as 180° away from the preferred direction.

Normalized tuning curves: Normalized tuning curves were calculated by first determining the cell's preferred direction (see above), and then dividing the response in all 8 stimulus directions to the response in that preferred direction. For cases in which the preferred direction did not match a stimulus direction that was specifically probed, the preferred direction response was estimated by a linear interpolation of the two neighboring probed directions. The area of the normalized tuning curve (abbreviated as the "normalized area") was calculated by dividing the area under the curve of the linear normalized tuning curve by 360°. The area of the normalized tuning curve is always greater than 0, but has no upper bound - though it tended to fall below 1. Larger values indicate a wider tuning curve. Perfectly circular tuning curves take a value of 1.

Direction selectivity index: The direction selectivity index (DSI) was calculated as the magnitude of the vector sum divided by the scalar sum of responses to all 8 stimulus directions. The direction selectivity index ranges between 0 and 1, with larger values indicating sharper tuning curves.

Von Mises fit: Tuning curves were fit to the Von Mises function by minimizing the sum of squared residuals. The Von Mises function is a circular analog of the Gaussian curve defined as $f(x) =$

832 $\frac{e^{\kappa cos(x-\mu)}}{2\pi I_0(\kappa)}$ [Eq. 3], where μ is the center of the curve, $1/\kappa$ controls the width of the curve, and I_0 is

833 the modified Bessel function of the first kind, of order 0. A larger κ value indicates a sharper fit.

834

835 **Retinal ganglion cell classification:** Retrogradely-labeled retinal ganglion cells were classified

836 as either Superior or Inferior oDSGCs if they had a direction selectivity index of greater than 0.05

837 and a preferred direction more than 30° off of the temporal-nasal axis, as calculated by spike

838 outputs measured in the cell-attached configuration. The vast majority of recorded cells met these

839 criteria, but those that did not were excluded from further analyses (**Fig S1**). All recorded cells in

840 our data set were dominated by ON responses to a light increment (**Fig S4**).

841

842 **Current injections:** Depolarizing or hyperpolarizing currents were continuously injected while

843 measuring voltages across stimulus directions in the current-clamp configuration. The magnitude

844 of current injections changed subtly from cell to cell depending on resting membrane potential,

845 input resistance, and spike threshold. On average, depolarizing current injections increased the

846 membrane potential by ~6mV (to ~-48mV), whereas hyperpolarizing current injections decreased

847 the membrane potential by ~6mV (to ~-60mV). Depolarizing injections were always small enough

848 such that the new resting membrane potential remained below spike threshold and each cell's

849 baseline firing rate was 0hz. The order of depolarizing and hyperpolarizing injections was random

850 across cells.

851

852 **Isolation of spikes and subthreshold voltages:** From current-clamp recordings, the onset and

853 offset of each action potential were determined using the first and second derivatives of the

854 voltage trace and a fixed minimum refractory period. The subthreshold voltage was then linearly

855 interpolated between action potential onsets and offsets.

856

857 **Subthreshold voltage tuning curves:** The maximum voltage deflection from baseline was used
858 to determine subthreshold membrane potential tuning curves. Values were averaged over 5
859 repetitions for each stimulus direction. Tuning curve metrics were calculated as for spikes.
860
861 **Electrophysiology at low contrast:** Low contrast drifting bars had an intensity of 0.5×10^4 S-cone
862 photoisomerizations/s (~5-fold dimmer than high contrast bars) from the same background of 124
863 S-cone photoisomerizations/s. All other stimulus parameters were equivalent across contrasts. In
864 a subset of cells, low contrast bars failed to elicit spikes for every stimulus direction. In such cases,
865 the cell's spike tuning curve area was set to 0, the area of its normalized tuning curve was set to
866 0, and its direction selectivity index was set to 1. We chose this convention because of the
867 observation that, across cells, as the total number of spikes approached 0, the area of the
868 normalized tuning curve approached 0 and the direction selectivity index approached 1. This
869 pattern also fits the prediction made by our leaky integrate-and-fire model (**Fig 7I**). Cells with no
870 responses under low contrast were classified as Superior or Inferior on the basis of their
871 responses to high contrast stimuli.
872
873 **Immunohistochemistry:** Individual ganglion cells were filled with either Lucifer yellow or biocytin
874 during electrophysiology experiments. Retinas were subsequently fixed in 2% paraformaldehyde
875 for 20 minutes at room temperature. The following protocol was used to enhance for the cell fills
876 [anti-Lucifer yellow (Life Technologies A5750) and/or streptavidin-488 (Thermo Fisher S11223)],
877 label synaptic puncta [anti-postsynaptic density (PSD-95, UC Davis NeuroMab 75-028), anti-
878 Gephyrin (Synaptic Systems 147 111)], and stain for cholinergic starburst amacrine cells [anti-
879 choline acetyltransferase (ChAT, Millipore AB144P)]: blocking serum (1 day), primary antibody
880 incubation (5 days), rinse 3x in PBS, secondary antibody (Jackson ImmunoResearch) incubation
881 (1 day), rinse 3x in PBS. Retinas were mounted with a spacer in vectashield (Vector labs) and
882 under a coverslip.

883

884 **Imaging:** Individual ganglion cells with known direction selectivity and their associated synaptic
885 puncta were imaged on a confocal microscope (Leica SP8). Ganglion cells were imaged with a
886 40x objective (NA 1.3) at a resolution of 0.102 x 0.102 x 0.3μm.

887

888 **Image analysis:** Confocal images were first median filtered in 3 dimensions (Fiji). Ganglion cell
889 dendrites were reconstructed using the filament function in Imaris (Oxford Instruments). Convex
890 polygons, dendritic branch numbers, and total dendritic length were obtained from the filaments.
891 Excitatory PSD-95 and inhibitory gephyrin puncta were identified and quantified within the filament
892 mask of the ganglion cell dendrites (ObjectFinder,
893 https://lucadellasantina.github.io/ObjectFinder/). Quantification of the puncta density from the
894 center to periphery and along dendritic depth were also obtained in ObjectFinder.

895

896 **Electrical properties of oDSGCs:** The resting membrane potential, spike threshold, and input
897 resistance of oDSGCs were all measured during whole-cell current-clamp recordings. Resting
898 membrane potential was taken as the initial membrane voltage immediately after establishing
899 intracellular access. Spike threshold and input resistance were both calculated by injecting a slow
900 ramp of current. Spike threshold was the average voltage at which a cell initiated its first action
901 potential in response to the ramp. Input resistance was calculated from the average slope of the
902 I-V response below spike threshold. Both metrics were averaged over at least 5 repetitions of the
903 ramp stimulus per cell. The membrane capacitance was measured during voltage-clamp
904 recordings using the built-in capacitance calculator from the MultiClamp 700B Amplifier (Axon
905 Instruments).

906

907 **Parallel conductance model:** We implemented a parallel conductance model in MATLAB to
908 build the model oDSGC (adopted from Antoine et al., 2019[98]). Excitatory (Gex) and inhibitory (Gin)

909 conductances were calculated at each time point for each direction of stimulus motion using
910 Ohm's law: $G = I/(Vhold - Erev)$ [Eq. 4], where I was the mean current trace recorded in
911 voltage-clamp across both Superior and Inferior cells, $Vhold$ was the holding potential, and $Erev$
912 was the reversal potential for either excitation or inhibition. A liquid junction potential of 5mV was
913 subtracted from $Vhold$ and $Erev$. Because our model called for directionally untuned excitation,
914 but the recorded excitatory conductances were slightly different for each direction of stimulus
915 motion (likely due to space-clamp error), we used an identical excitatory conductance for all
916 directions of stimulus motion that was equal to the maximum conductance at each time point
917 across all recorded directions (space-clamp errors reduce empirically recorded excitatory currents
918 in voltage-clamp mode). The excitatory conductance was then multiplied by a gain value to
919 achieve a final time series for Gex. Next, we used the equation

920 $C\frac{dV}{dt} = Gex(Eex - Vm) + Gin(Ein - Vm) + Grest(Erest - Vm)$ [Eq. 5]

921 to determine the membrane potential at each time point. C was the median capacitance of
922 Superior and Inferior oDSGCs as measured during whole-cell recordings. $Grest$ was the
923 reciprocal of the median input resistance, which we calculated by injecting a slow ramp of current
924 in a subset of recorded cells and determining the average slope of the I-V response below spike
925 threshold. $Erest$ was the median resting membrane potential. Vm was calculated at each point
926 in time by initializing it at $Erest$, and then determining each subsequent value using Euler's
927 method and an integration time step of 1ms. The peak change in this Vm value above $Erest$ was
928 used to construct the Vm tuning curves in the version of the model without a spiking component.

929 In the version of the model with a spiking component, we again solved for Vm at every
930 time point using Euler's method. In this case, however, whenever Vm surpassed the threshold
931 potential, a "spike" was counted and a 3ms pause corresponding to the spike time and refractory
932 period was initiated, after which Vm was reset to $Erest$ and the process continued. The threshold
933 value was fixed such that the the normalized area and direction selectivity index of the model

934 oDSGC's spike tuning curve matched the median empirical values for these metrics (taken from
935 cell-attached recordings) when the excitatory gain was set to 1.0. This resulted in a threshold
936 value of -46.2mV, which was 2.9mV more negative than the median empirically recorded spike
937 threshold.

938 Because resetting Vm to $Erest$ after each spike also changed the driving forces for
939 excitation and inhibition - and therefore possibly the shape of resulting spike tuning curves - we
940 also simulated spike responses by assuming that the number of spikes produced to a given
941 stimulus was linearly proportional to the amount of time that Vm (calculated without a spiking
942 mechanism in place) spent above spike threshold (data not shown). Results from this model were
943 not substantively different than those from the model in which a refractory period was included
944 and Vm was reset to $Erest$ after each spike.

945 This same model was used to test the contrast-dependence of spike and Vm tuning
946 curves. In this case, both the excitatory and each of the 8 inhibitory conductance time series were
947 multiplied by the gain value to calculate Gex and Gin, respectively.

948

949 **Behavioral predictions from oDSGC activity:** Predictions for OKR gain were calculated on the
950 basis of the difference in median firing rates between Superior and Inferior oDSGC populations.
951 The preferred and null directions of each cell in our dataset were computed in response to a high
952 contrast drifting bar. Gain predictions were made under each stimulus condition by (1) resampling
953 from distributions of oDSGC responses for that condition 10,000 times, (2) computing the
954 difference (i.e., delta) between the median preferred and null direction responses on each iteration
955 for the appropriate cell types, and (3) using the median of these bootstrapped distributions of delta
956 as an estimate of relative gain.

957 Computing the preferred and null direction of each cell has the advantage of controlling
958 for the fact that the observed preferred direction of individual oDSGCs can change based on
959 retinotopic location when the retina is flatmounted[16]. Assigning the preferred direction to a

960 constant stimulus direction across cells (e.g. dorsal-to-ventral motion on the retina for Superior
961 oDSGCs) did not change the behavioral predictions (data not shown).
962
963 **Empirical nonlinearity:** oDSGC spike outputs were related to OKR gain by computing an
964 empirical nonlinearity using the Hill equation, defined as $g(r) = g_{min} + \frac{g_{max} - g_{min}}{1+(\frac{r_{1/2}}{r})^n}$ [Eq. 6], where
965 g_{min} is the minimum OKR gain value, g_{max} is the maximum OKR gain value, $r_{1/2}$ is the ganglion
966 cell response (defined as the difference between Superior and Inferior oDSGC firing rates) that
967 corresponds to 50% of g_{max}, and n sets the steepness of the curve. g_{min} was fixed at 0 such that
968 the nonlinearity would predict a gain of 0 for an oDSGC response of 0. g_{max} was fixed at 1.0 such
969 that the nonlinearity would not predict gains above 1.0. The empirical nonlinearity was then
970 determined by using a least-squares fit of Eq. 6 to the four measured data points (oDSGC
971 responses and OKR gain values measured for superior/inferior stimuli at high/low contrast).
972
973
974 **ACKNOWLEDGEMENTS**
975
976 We would like to thank Connie Chen and Jeremiah John for technical assistance; Kevin Bender,
977 David Copenhagen, Daniel Denman, Tonatiuh Garcia Ruiz, Jonathan Horton, Jeanette Hyer,
978 David Kastner, Joo Yeun Lee, Yien Ming-Kuo, Satoru Miura, Yvonne Ou, Luca Della Santina,
979 Massimo Scanziani, Manuel Solino, and Alfred Yu for helpful discussions; David Berson, Guy
980 Bouvier, and Fred Rieke for comments on the manuscript. This work was supported by NIH
981 through F31 EY-033225 (S.C.H.), R01 EY-029772 (F.A.D.), R01 EY-030136 (F.A.D.), and the
982 Vision Core Grant P30 EY-002162 (UCSF), internally by the Moritz-Heyman Discovery Fellowship
983 (S.C.H.) and the Kavli Institute for Neuroscience (UCSF), and through foundation grants from the

McKnight Scholar Award (F.A.D.), Research to Prevent Blindness (Unrestricted Grant), and That Man May See.

AUTHOR CONTRIBUTIONS

Both authors conceptualized the project, designed experiments, and constructed experimental rigs. S.C.H. conducted and analyzed the behavioral and electrophysiological experiments and performed the modeling. F.A.D. conducted and analyzed the confocal imaging. Both authors wrote the manuscript and acquired funding and resources.

COMPETING INTERESTS

The authors declare no competing interests.

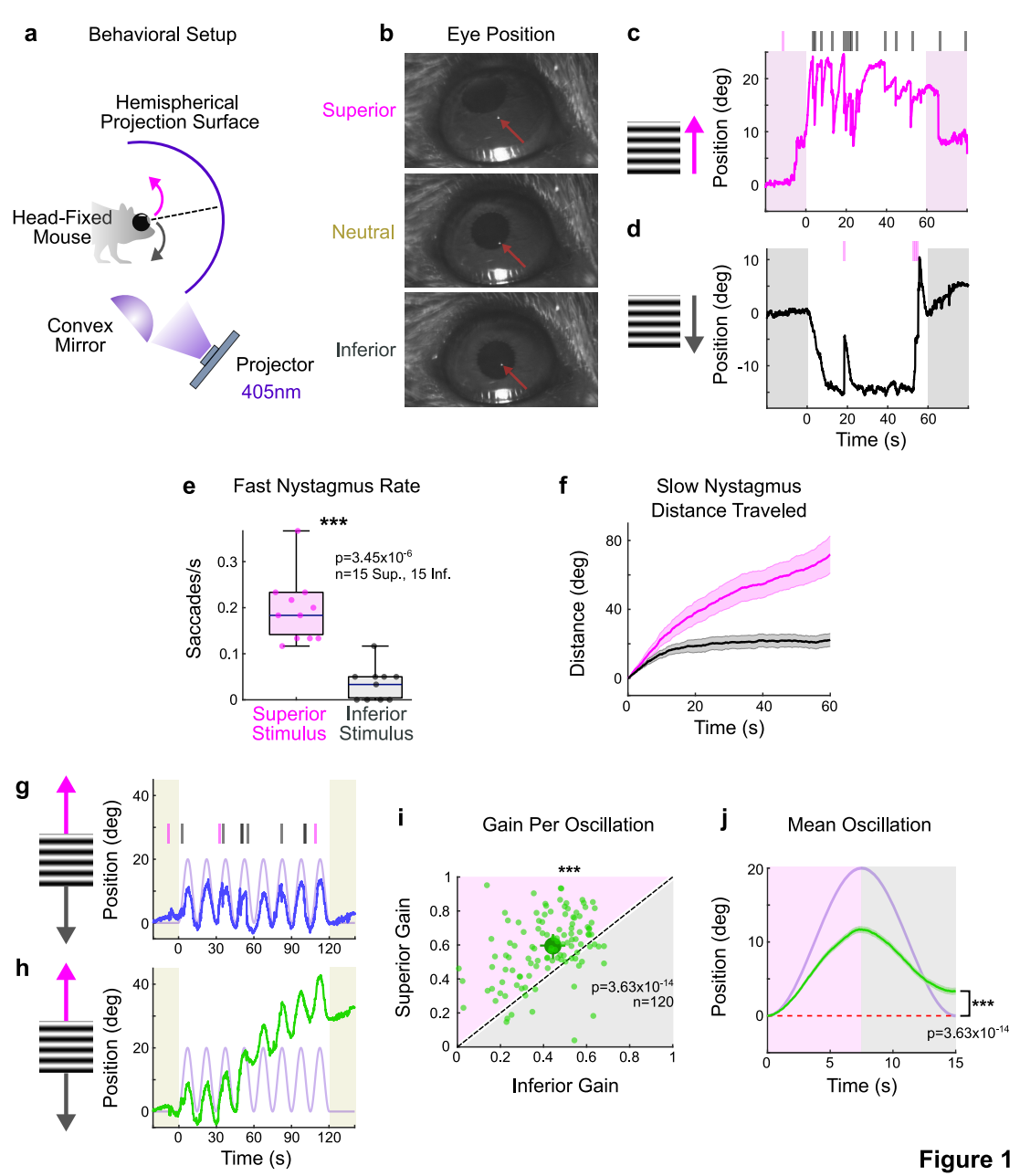
a
Behavioral Setup
Hemispherical Projection Surface
Head-Fixed Mouse
Convex Mirror
Projector
405nm
b
Eye Position
Superior
Neutral
Inferior
c
Position (deg)
d
Position (deg)
Time (s)
e
Fast Nystagmus Rate
***
p=3.45x10-6
n=15 Sup., 15 Inf.
Saccades/s
Superior Stimulus
Inferior Stimulus
f
Slow Nystagmus Distance Traveled
Distance (deg)
Time (s)
g
Position (deg)
h
Position (deg)
Time (s)
i
Gain Per Oscillation
***
p=3.63x10-14
n=120
Superior Gain
Inferior Gain
j
Mean Oscillation
Position (deg)
***
p=3.63x10-14
Time (s)

Figure 1

999 **Figure 1. Superior and inferior OKR are asymmetric in adult mice. (a)** Schematic of
1000 behavioral setup to elicit the vertical optokinetic reflex (OKR). The mouse is situated so that one
1001 eye is centered in a hemisphere. Stimuli are projected onto the hemisphere's concave surface via
1002 reflection off of a convex mirror. Eye movements are tracked using an infrared-sensitive camera
1003 and corneal reflection (see Methods). **(b)** Example video frames demonstrating that the eye
1004 traverses between superior, neutral, and inferior positions in the presence of vertically-drifting
1005 sinusoidal gratings. Red arrows mark the infrared corneal reflection. **(c-d)** Vertical angle of the
1006 eye across an example epoch in response to full-contrast **(c)** superior and **(d)** inferior drifting
1007 gratings (10°/s). For each epoch, a continuous 60s stimulus was flanked by 20s of a static grating
1008 (shaded regions). Ticks above the plots mark the time of fast nystagmus either in the superior
1009 (magenta) or inferior (gray) direction. Examples from one animal. **(e)** Rate of vertical fast
1010 nystagmus for superior and inferior stimuli. Horizontal line represents median, box boundaries are
1011 the IQR, whiskers represent most extreme observation within 1.5xIQR. **(f)** Cumulative vertical
1012 distance traveled during slow nystagmus in response to superior (magenta) and inferior (gray)
1013 drifting gratings after removing fast nystagmuses (mean±SEM). **(g-h)** Eye position in response to
1014 a grating oscillating sinusoidally along the vertical axis. For each epoch, a continuous 120s
1015 stimulus, consisting of 8 oscillation cycles, was flanked by 20s of a static grating (shaded regions).
1016 Stimulus position in lavender. **(g)** Raw vertical eye position (blue) including the presence of fast
1017 nystagmuses (ticks). **(h)** Eye position after removing fast nystagmuses (green). **(i)** Average gain
1018 of slow nystagmus during the superior versus inferior phase of individual oscillations. Each small
1019 dot is a single oscillation. The region of magenta [or gray] indicates that gain was greater for the
1020 superior [or inferior] phase of the oscillation. Points that fall on the line indicate equivalent gain for
1021 both stimulus directions. Large point and whiskers represent univariate medians and 95%
1022 confidence intervals (via bootstrapping), respectively. Significance value indicates whether the
1023 points tend to fall unevenly on one side of the unity line (2-sided signed-rank). **(j)** Eye position
1024 (green) and stimulus position (lavender) averaged across all oscillations and all animals

1025 (mean±SEM). Starting eye position is normalized to 0° at cycle onset. The average ending eye
1026 position is displaced in the superior direction (2-sided signed-rank). N=5 mice for all experiments;
1027 n=number of trials. See also Fig S6.

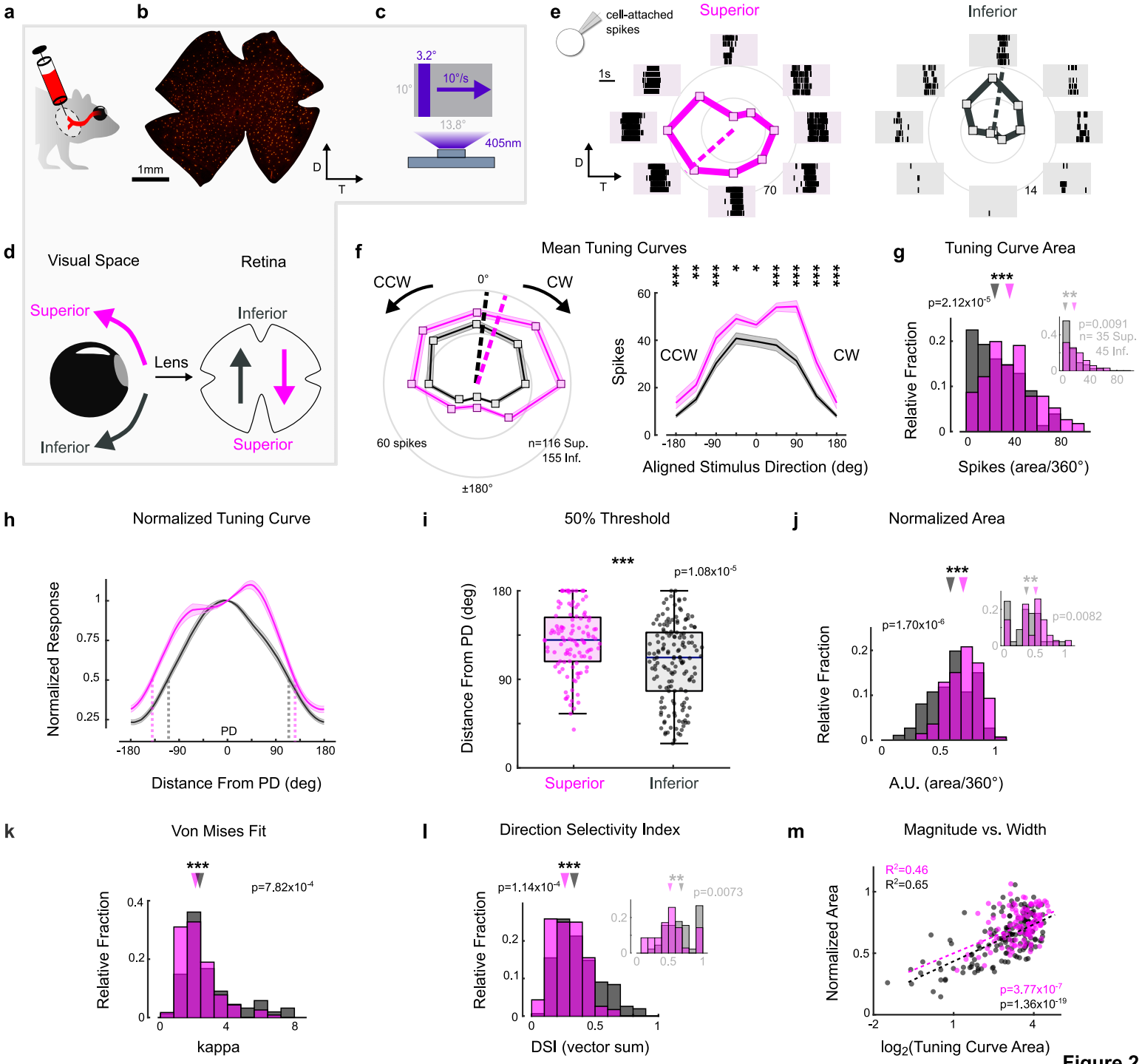
a
b
c
1mm
D
T
3.2°
10°
10°/s
13.8°
405nm
e
cell-attached spikes
Superior
Inferior
1s
70
14
d
Visual Space
Retina
Superior
Inferior
Lens
Inferior
Superior
f
Mean Tuning Curves
CCW
CW
0°
60 spikes
n=116 Sup.
155 Inf.
±180°
Spikes
Aligned Stimulus Direction (deg)
g
Tuning Curve Area
p=2.12x10^-5
p=0.0091
n= 35 Sup.
45 Inf.
Relative Fraction
Spikes (area/360°)
h
Normalized Tuning Curve
Normalized Response
PD
Distance From PD (deg)
i
50% Threshold
p=1.08x10^-5
Distance From PD (deg)
Superior
Inferior
j
Normalized Area
p=1.70x10^-6
p=0.0082
Relative Fraction
A.U. (area/360°)
k
Von Mises Fit
p=7.82x10^-4
Relative Fraction
kappa
l
Direction Selectivity Index
p=1.14x10^-4
p=0.0073
Relative Fraction
DSI (vector sum)
m
Magnitude vs. Width
R²=0.46
R²=0.65
p=3.77x10^-7
p=1.36x10^-19
Normalized Area
log2(Tuning Curve Area)

Figure 2

1028 **Figure 2. Superior and Inferior oDSGCs have asymmetric spike tuning curves**. **(a)**
1029 Schematic illustrating unilateral bead injections into medial terminal nucleus (MTN) to retrogradely
1030 label ganglion cells in the contralateral retina. **(b)** Flat-mount retina with retrogradely labeled,
1031 MTN-projecting ganglion cells. **(c)** Drifting bar stimulus (3.2° x limiting projector dimension, 10°/s,
1032 2.4×10^4 S-cone photoisomerization/s). **(d)** Definitions of superior (magenta) and inferior (gray)
1033 motion in visual space and on the retina. Directions are inverted by the lens. **(e)** Cell-attached
1034 spikes from labeled retinal ganglion cells in a flat-mount retina in response to a bar drifting in 8
1035 directions. Spike responses and average tuning curves from an example Superior (left, magenta)
1036 and Inferior (right, gray) oDSGC. Mean spike counts are presented as the distance from the origin,
1037 marked by concentric circles. Numbers on circles indicate spike counts. Dashed lines represent
1038 the preferred direction of each cell, calculated as the direction of the vector sum of all responses.
1039 Coordinates are in retinal space. **(f)** Population tuning curves across all Superior and Inferior
1040 oDSGCs (mean±SEM). Left: polar plots [as in (e)] aligned by rotating the tuning curves of Superior
1041 cells by 180°. Right: linear representation of the same data (referred to as the "linear tuning
1042 curve"). CW: clockwise; CCW: counterclockwise. 0° represents directly superior/inferior motion.
1043 **(g)** Histograms of the area under the curve of the linear tuning curve of every cell. Inset shows
1044 the same metric for a stimulus at 5-fold lower contrast. **(h)** Population mean (±SEM) normalized
1045 tuning curves - computed by normalizing and aligning (at 0°) the response of each cell to its
1046 response in the preferred direction. Vertical dashed lines indicate the point at which mean
1047 response magnitudes drop below 50% of the preferred direction response. **(i)** Distributions of the
1048 distance (in degrees) from each cell's preferred direction to the point at which its response
1049 magnitude crosses the 50% threshold [dashed lines in (h)]. Horizontal line represents median,
1050 box boundaries are the IQR, whiskers represent most extreme observation within 1.5xIQR. Points
1051 represent individual cells. **(j)** Histograms of the area under the curve of the normalized tuning
1052 curve [as in (h)] of every cell (abbreviated as "normalized area"). A larger normalized area
1053 indicates a broader tuning curve (see Methods). Inset shows the same metric for a stimulus at 5-

1054 fold lower contrast. **(k)** Histograms of the kappa parameter for the Von Mises fit of the tuning curve
1055 of every cell (see Methods). A smaller kappa value indicates that the fit is wider. **(l)** Histograms of
1056 the direction selectivity index (DSI, vector sum, see Methods) of every cell. Inset shows the same
1057 metric for a stimulus at 5-fold lower contrast. **(m)** Linear tuning curve area, i.e. “magnitude,” [as
1058 in (g)] versus area of the normalized tuning curve, i.e., “width,” [as in (j)] were positively correlated
1059 on a cell-by-cell basis for both Superior and Inferior oDSGCs. For all histograms, medians of
1060 Superior (magenta) and Inferior (gray) oDSGC distributions are indicated by arrows. *$p<0.05$,
1061 **$p<0.01$, ***$p<0.001$. See also Fig S1, S2, S3.

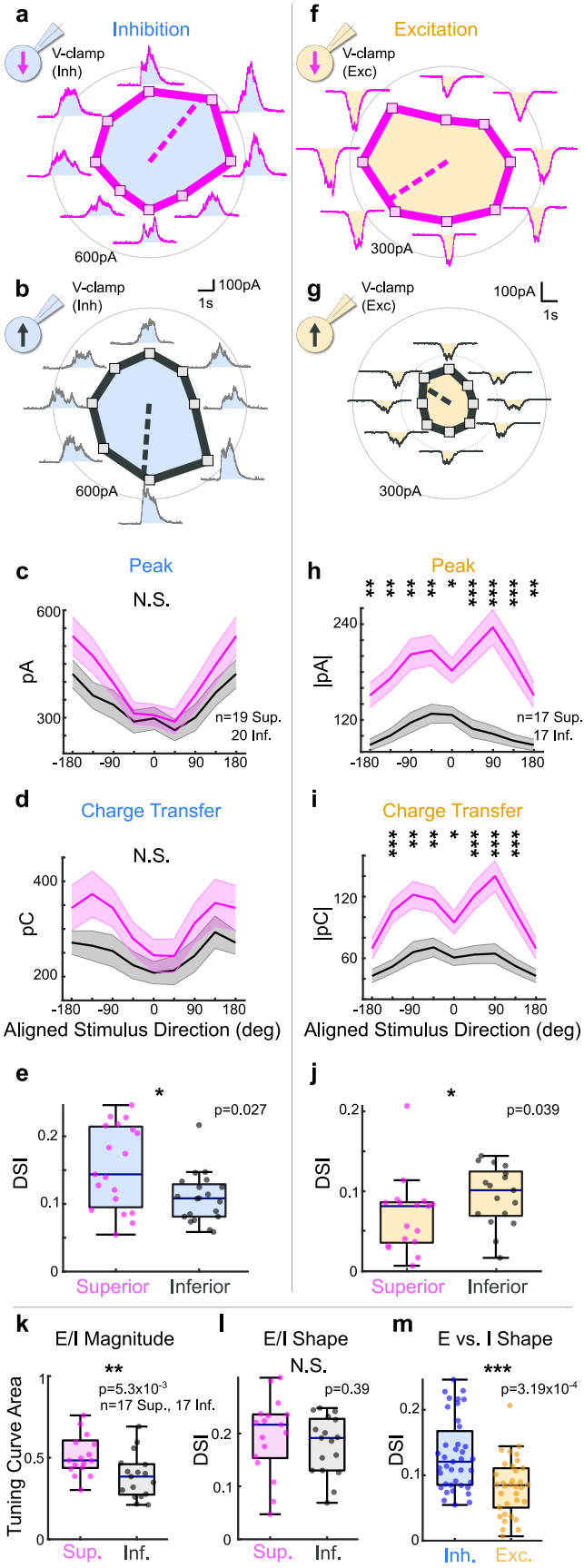
a
Inhibition
V-clamp
(Inh)
600pA
b
V-clamp
(Inh)
100pA
1s
600pA
f
Excitation
V-clamp
(Exc)
300pA
g
V-clamp
(Exc)
100pA
1s
300pA
c
Peak
N.S.
pA
600
300
n=19 Sup.
20 Inf.
-180 -90 0 90 180
h
Peak
|pA|
240
120
n=17 Sup.
17 Inf.
-180 -90 0 90 180
d
Charge Transfer
N.S.
pC
400
200
-180 -90 0 90 180
Aligned Stimulus Direction (deg)
i
Charge Transfer
|pC|
120
60
-180 -90 0 90 180
Aligned Stimulus Direction (deg)
e
DSI
0.2
0.1
0
*
p=0.027
Superior
Inferior
j
DSI
0.2
0.1
0
*
p=0.039
Superior
Inferior
k
E/I Magnitude
Tuning Curve Area
1
0.5
0
**
p=5.3x10-3
n=17 Sup., 17 Inf.
Sup.
Inf.
l
E/I Shape
N.S.
DSI
0.2
0.1
0
p=0.39
Sup.
Inf.
m
E vs. I Shape
DSI
0.2
0.1
0
***
p=3.19x10-4
Inh.
Exc.

Figure 3

1062 **Figure 3. Superior oDSGCs receive similar inhibitory inputs but greater excitatory inputs**
1063 **compared to Inferior oDSGCs. (a)** Inhibitory currents measured from an exemplar Superior
1064 oDSGC under voltage-clamp at +10mV in response to a bar drifting in 8 directions. **(b)** Same as
1065 (a) for an exemplar Inferior oDSGC. **(c-d)** Population responses for inhibitory currents. Stimulus
1066 direction is on the abscissa and **(c)** peak inhibitory current or **(d)** total inhibitory charge transfer is
1067 on the ordinate for Superior (magenta) and Inferior (gray) oDSGCs (mean±SEM). Stimulus
1068 directions are aligned across cell types, where 0° indicates directly superior (for Superior
1069 oDSGCs) or inferior (for Inferior oDSGCs) motion. Positive directions are clockwise. **(e)**
1070 Distributions of the direction selectivity index for peak inhibitory currents in individual Superior and
1071 Inferior oDSGCs. **(f)** Excitatory currents measured from an exemplar Superior oDSGC under
1072 voltage-clamp at -60mV in response to a bar drifting in 8 directions. Same cell as in (a). **(g)** Same
1073 as (f) for an exemplar Inferior oDSGC. Same cell as in (b). **(h-i)** Population responses for
1074 excitatory currents. Aligned stimulus direction is on the abscissa and **(h)** peak excitatory current
1075 or **(d)** total excitatory charge transfer is on the ordinate for Superior (magenta) and Inferior (gray)
1076 oDSGCs (mean±SEM). **(j)** Distributions of the direction selectivity index for peak excitatory
1077 currents in individual Superior and Inferior oDSGCs. **(k-l)** The ratio of the peak excitatory current
1078 to the peak inhibitory current (E/I) was calculated for each stimulus direction for cells in which
1079 both metrics were recorded. **(k)** Distributions of the linear tuning curve area of E/I. Arbitrary units
1080 (E/I/360°). **(l)** Distributions of the direction selectivity index for E/I. **(m)** Direction selectivity index
1081 for peak inhibitory (blue) and excitatory (yellow) currents collapsed across Superior and Inferior
1082 oDSGCs. For box plots, horizontal line represents median, box boundaries are IQR, and whiskers
1083 represent most extreme observation within 1.5xIQR. *$p<0.05$, **$p<0.01$, ***$p<0.001$. See also Fig
1084 S3, S4.

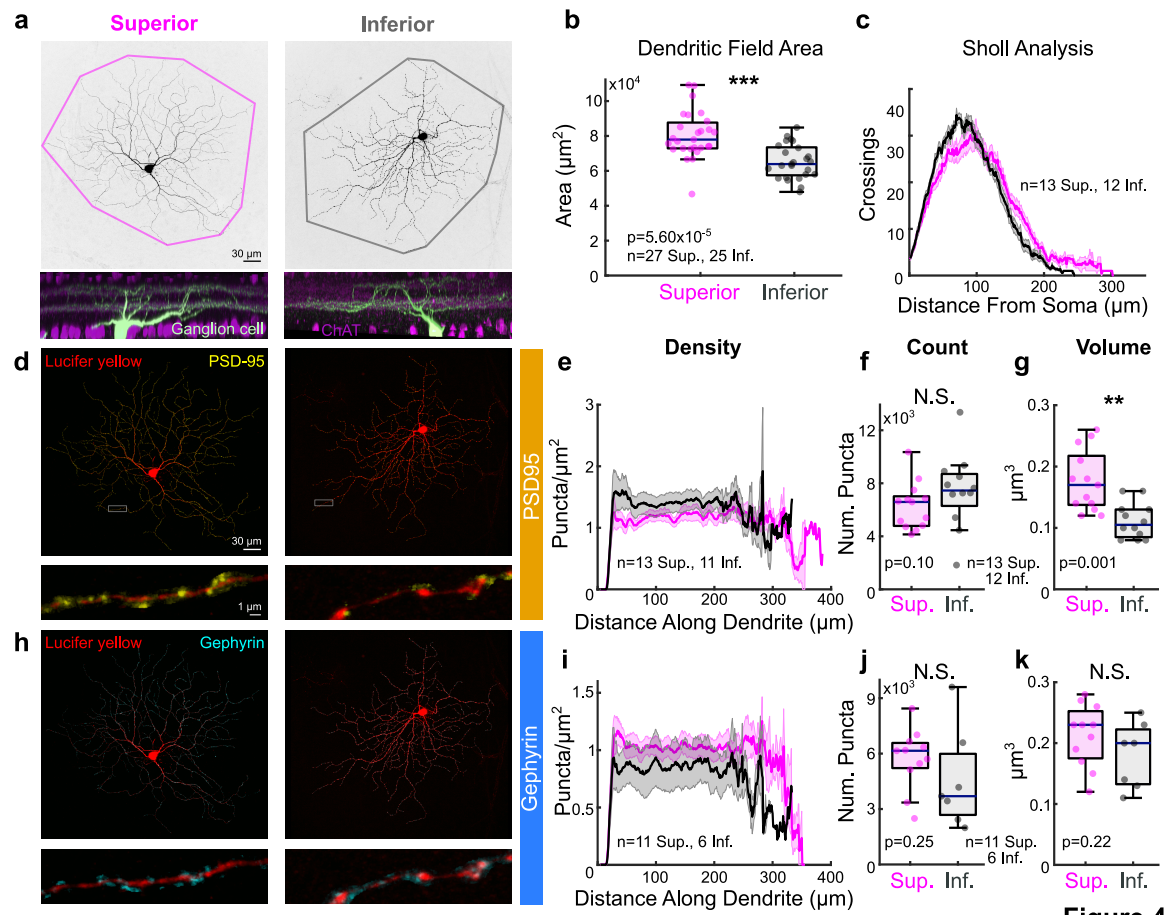
a
Superior
Inferior
30 µm
Ganglion cell
ChAT
b
Dendritic Field Area
x10^4
***
Area (µm^2)
p=5.60x10^-5
n=27 Sup., 25 Inf.
Superior
Inferior
c
Sholl Analysis
Crossings
n=13 Sup., 12 Inf.
Distance From Soma (µm)
d
Lucifer yellow
PSD-95
30 µm
1 µm
PSD95
e
Density
Puncta/µm^2
n=13 Sup., 11 Inf.
Distance Along Dendrite (µm)
f
Count
N.S.
x10^3
Num. Puncta
p=0.10
n=13 Sup.
12 Inf.
Sup.
Inf.
g
Volume
**
µm^3
p=0.001
Sup.
Inf.
h
Lucifer yellow
Gephyrin
Gephyrin
i
Puncta/µm^2
n=11 Sup., 6 Inf.
Distance Along Dendrite (µm)
j
N.S.
x10^3
Num. Puncta
p=0.25
n=11 Sup.
6 Inf.
Sup.
Inf.
k
N.S.
µm^3
p=0.22
Sup.
Inf.

Figure 4

1085 **Figure 4. Superior oDSGCs have greater dendritic fields and larger excitatory postsynaptic**
1086 **sites. (a)** Confocal images of a Superior (left) and Inferior (right) oDSGC filled with dye. Convex
1087 polygons are drawn around the tips of their dendrites. (Bottom) Side views of different Superior
1088 and Inferior oDSGCs filled and stained for acetylcholinesterase (ChAT) bands. Both cell types
1089 have dendrites that stratify in the ON and OFF ChAT bands, with the majority of dendrites in the
1090 ON sublamina. **(b)** Convex polygon areas across cells. **(c)** Sholl analysis indicating the number
1091 of dendritic crossings as a function of radial distance from the soma (mean±SEM). **(d, h)** Ganglion
1092 cells with immunostaining for **(d)** excitatory postsynaptic scaffolding protein PSD-95 or **(h)**
1093 inhibitory postsynaptic scaffolding protein gephyrin. (Bottom) Magnification of a stretch of
1094 dendrites with labeled puncta. **(e, i)** Quantification of puncta density as a function of distance
1095 along the dendrite for **(e)** PSD-95 and **(i)** gephyrin (mean±SEM). **(f, j)** Total number of puncta
1096 within each ganglion cell for **(f)** PSD-95 and **(j)** gephyrin. **(g, k)** Quantification of average puncta
1097 volume for **(g)** PSD-95 and **(k)** gephyrin. For box plots, horizontal line represents median, box
1098 boundaries are IQR, and whiskers represent most extreme observation within 1.5xIQR. *$p<0.05$,
1099 **$p<0.01$, ***$p<0.001$. See also Fig S3, S4.

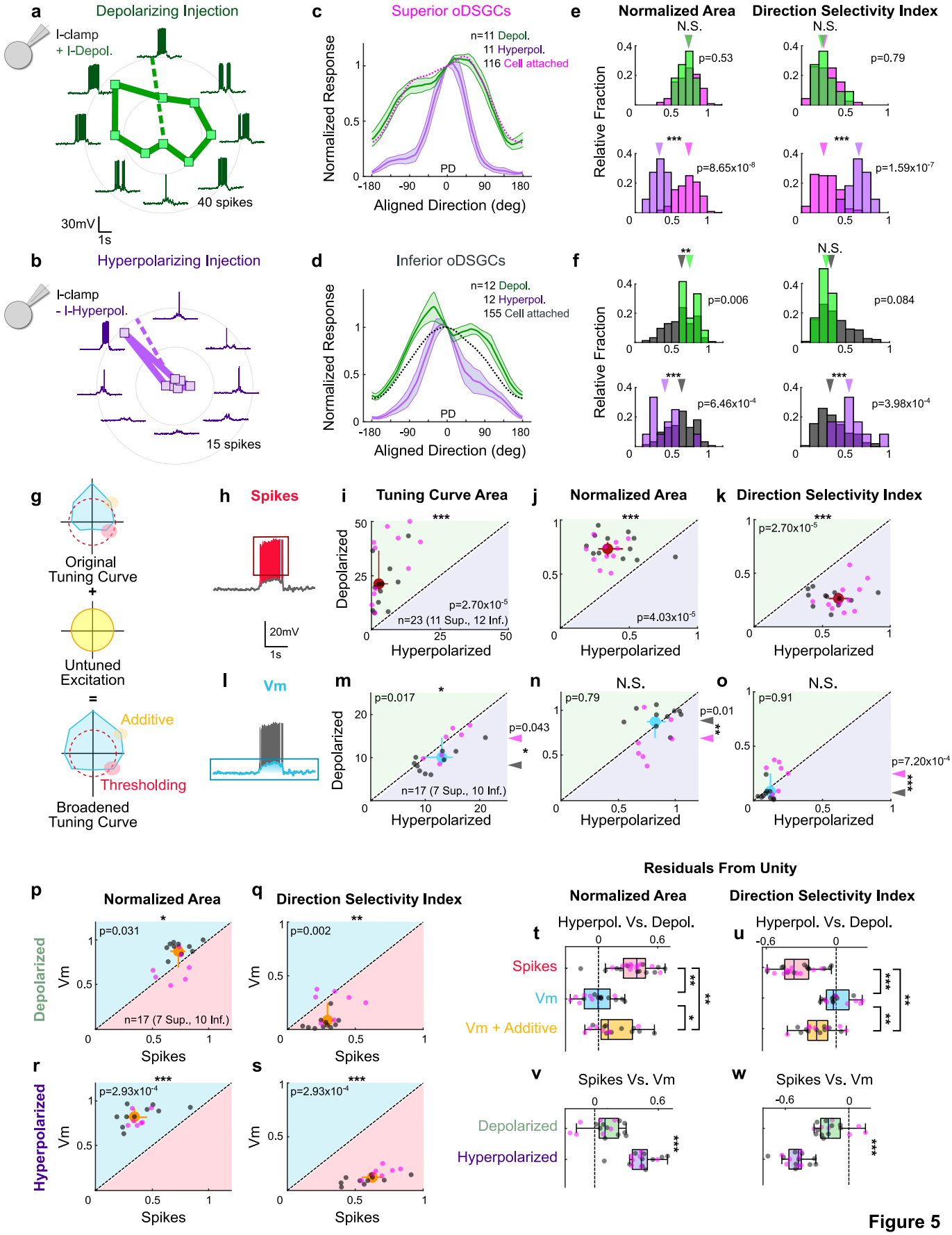
a
Depolarizing Injection
I-clamp
+ I-Depol.
40 spikes
30mV
1s
b
Hyperpolarizing Injection
I-clamp
- I-Hyperpol.
15 spikes
c
Superior oDSGCs
n=11 Depol.
11 Hyperpol.
116 Cell attached
Normalized Response
PD
Aligned Direction (deg)
d
Inferior oDSGCs
n=12 Depol.
12 Hyperpol.
155 Cell attached
Normalized Response
PD
Aligned Direction (deg)
e
Normalized Area
Direction Selectivity Index
N.S.
p=0.53
p=0.79
p=8.65x10^-8
p=1.59x10^-7
Relative Fraction
f
p=0.006
p=0.084
p=6.46x10^-4
p=3.98x10^-4
Relative Fraction
g
Original Tuning Curve
Untuned Excitation
Additive
Thresholding
Broadened Tuning Curve
h
Spikes
20mV
1s
i
Tuning Curve Area
Depolarized
Hyperpolarized
p=2.70x10^-5
n=23 (11 Sup., 12 Inf.)
j
Normalized Area
Hyperpolarized
p=4.03x10^-5
k
Direction Selectivity Index
p=2.70x10^-5
Hyperpolarized
l
Vm
m
p=0.017
p=0.043
n=17 (7 Sup., 10 Inf.)
Depolarized
Hyperpolarized
n
N.S.
p=0.79
p=0.01
Hyperpolarized
o
N.S.
p=0.91
p=7.20x10^-4
Hyperpolarized
p
Normalized Area
Depolarized
p=0.031
n=17 (7 Sup., 10 Inf.)
Vm
Spikes
q
Direction Selectivity Index
p=0.002
Vm
Spikes
r
Hyperpolarized
p=2.93x10^-4
Vm
Spikes
s
p=2.93x10^-4
Vm
Spikes
Residuals From Unity
Normalized Area
Direction Selectivity Index
t
Hyperpol. Vs. Depol.
Spikes
Vm
Vm + Additive
u
Hyperpol. Vs. Depol.
v
Spikes Vs. Vm
Depolarized
Hyperpolarized
w
Spikes Vs. Vm

Figure 5

1100 **Figure 5. The spike threshold differentiates the tuning properties of Superior and Inferior**
1101 **oDSGCs. (a-b)** Exemplar Inferior oDSGC in whole-cell current-clamp during **(a)** depolarizing and
1102 **(b)** hyperpolarizing current injection in response to a bar moving in 8 directions. **(c-d)** Mean
1103 (±SEM) normalized tuning curves (aligned and normalized to the response of each cell in its
1104 preferred direction) for **(c)** Superior and **(d)** Inferior oDSGCs under conditions of depolarizing
1105 (green) and hyperpolarizing (purple) current injection. Dotted lines indicate the average
1106 normalized spike tuning curves of each population from cell-attached recordings (as in Fig 2h).
1107 **(e)** For Superior oDSGCs, histograms of the area of the normalized tuning curve (left) and
1108 direction selectivity index (right) under conditions of no current injection (i.e. cell-attached,
1109 magenta), depolarizing injection (top, green), and hyperpolarizing injection (bottom, purple). **(f)**
1110 Same as (e) for Inferior oDSGCs. Gray histograms represent cell-attached recordings. **(g)**
1111 Illustration of the influence of untuned excitation on the tuning curve through additive (yellow) and
1112 thresholding (red) effects. The blue area indicates the membrane potential and the dashed red
1113 line indicates the spike threshold. **(h, l)** Example whole-cell current-clamp recording in which **(h)**
1114 spikes and **(l)** subthreshold voltages (Vm) have been separated. **(i-k, m-o)** Scatter plots of tuning
1115 curve metrics during hyperpolarizing (abscissa) and depolarizing (ordinate) current injections for
1116 **(i-k)** spikes and **(m-o)** subthreshold voltages measured simultaneously: **(i, m)** linear tuning curve
1117 area, **(j, n)** area of the normalized tuning curve, **(k, o)** direction selectivity index. Regions of green
1118 [or purple] indicate that the metric is greater during depolarizing [or hyperpolarizing] injections.
1119 Points that fall on the line indicate equivalent metrics under the two conditions. Individual cells are
1120 shown as dots (Superior in magenta, Inferior in gray). Red and blue circles represent univariate
1121 medians (collapsed across cell type) and whiskers indicate 95% confidence intervals determined
1122 via bootstrapping. Significance values indicate whether the data tend to fall unevenly on one side
1123 of the unity line (2-sided signed-rank). Arrowheads in (m-o) represent the median of Superior
1124 (magenta) and Inferior (gray) oDSGCs along the line of slope unity, and associated significance
1125 values indicate comparison between Superior and Inferior oDSGCs (2-sided rank-sum). **(p-s)**

Tuning curve metrics for spikes (abscissa) and simultaneously measured subthreshold voltages (ordinate) under **(p-q)** depolarizing and **(r-s)** hyperpolarizing conditions: **(p, r)** area of the normalized tuning curve, and **(q, s)** direction selectivity index. Significance values indicate whether the data tend to fall unevenly on one side of the unity line (2-sided signed-rank). **(t-u)** Residuals from the unity line for individual cells from the plots in **(t)** (j) and (n) and **(u)** (k) and (o). Dashed line indicates unity (i.e. no difference across depolarizing and hyperpolarizing conditions). **(v-w)** Residuals from the unity line for individual cells from the plots in **(v)** (p) and (r) and **(w)** (q) and (s). Dashed line indicates unity (i.e., no difference between spikes and subthreshold voltages). Comparisons in (t-w) are made between conditions (2-sided rank-sum). For box plots, the blue line represents median, box boundaries are IQR, and whiskers represent most extreme observation within 1.5xIQR. *$p<0.05$, **$p<0.01$, ***$p<0.001$. See also Fig S5.

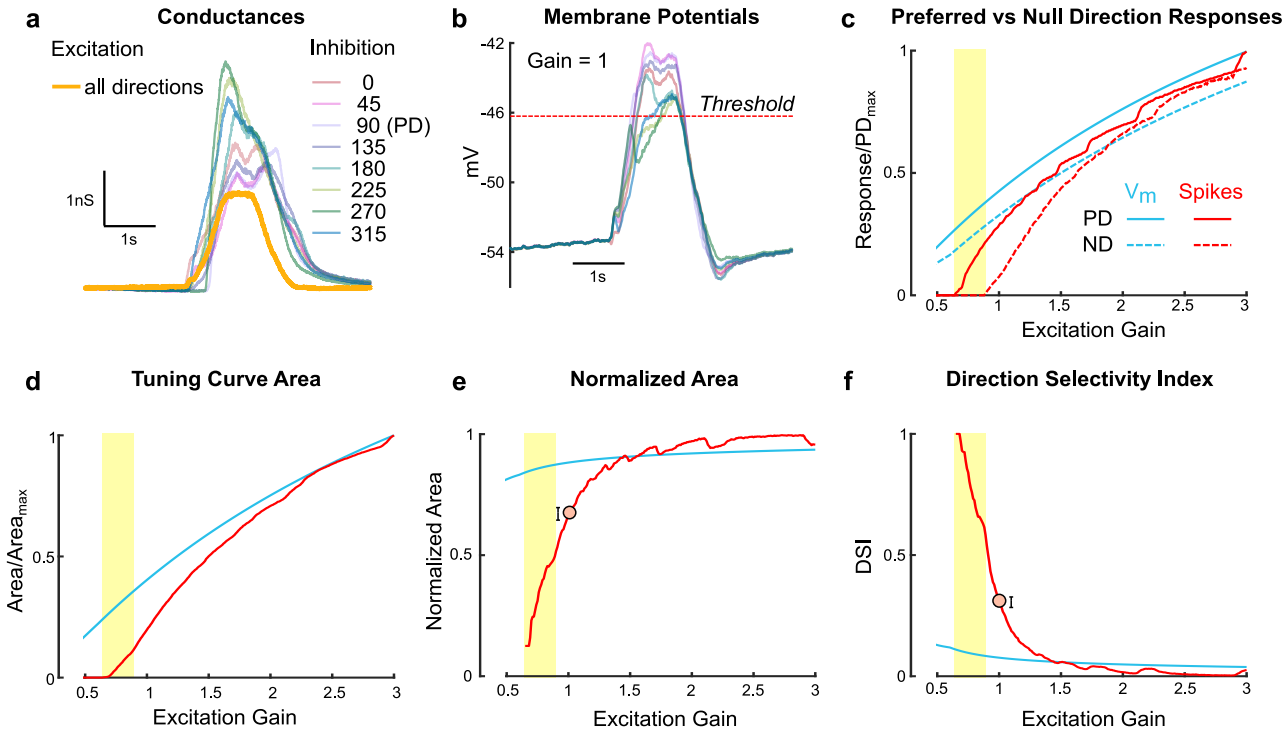
a
Conductances
Excitation
all directions
Inhibition
0
45
90 (PD)
135
180
225
270
315
1nS
1s
b
Membrane Potentials
Gain = 1
Threshold
mV
-42
-46
-50
-54
1s
c
Preferred vs Null Direction Responses
Response/PD$_{max}$
Vm
Spikes
PD
ND
Excitation Gain
d
Tuning Curve Area
Area/Area$_{max}$
Excitation Gain
e
Normalized Area
Normalized Area
I
Excitation Gain
f
Direction Selectivity Index
DSI
I
Excitation Gain

Figure 6

1137 **Figure 6. A leaky integrate-and-fire model demonstrates how untuned excitation**
1138 **contributes to direction tuning**. An exemplar oDSGC was modeled using parameters recorded
1139 directly from cells, including directionally tuned inhibitory conductances for each drifting bar
1140 direction, and a single, untuned excitatory conductance (see Methods). **(a)** Inhibitory (pastel
1141 colors) and excitatory (yellow) conductances of the model oDSGC in response to bars moving in
1142 8 directions. **(b)** The leaky integrate-and-fire model uses the empirically measured parameters to
1143 model membrane potential across bar directions, shown here for the case in which the excitatory
1144 gain (i.e. a multiplication factor applied to the excitatory conductance) is set to 1.0. The red dotted
1145 line indicates the spike threshold. **(c)** Preferred (solid lines) and null (dotted lines) direction
1146 responses of subthreshold voltages (blue) and spikes (red) across a range of excitatory gains.
1147 Values are normalized to the maximum preferred direction response for each metric. The yellow
1148 column indicates the regime in which the null direction elicits zero spikes but the preferred
1149 direction has nonzero spikes. **(d-f)** Directional tuning properties as a function of excitatory gain
1150 for subthreshold voltages (blue) and spikes (red): **(d)** area of the linear tuning curve (normalized
1151 to the maximum area for each metric), **(e)** area of the normalized tuning curve, and **(f)** direction
1152 selectivity index. Orange dots [and error bars] in (e) and (f) correspond to the empirically
1153 measured median [and 95% confidence intervals determined via bootstrapping] for each metric
1154 from cell-attached recordings, collapsed across cell types.

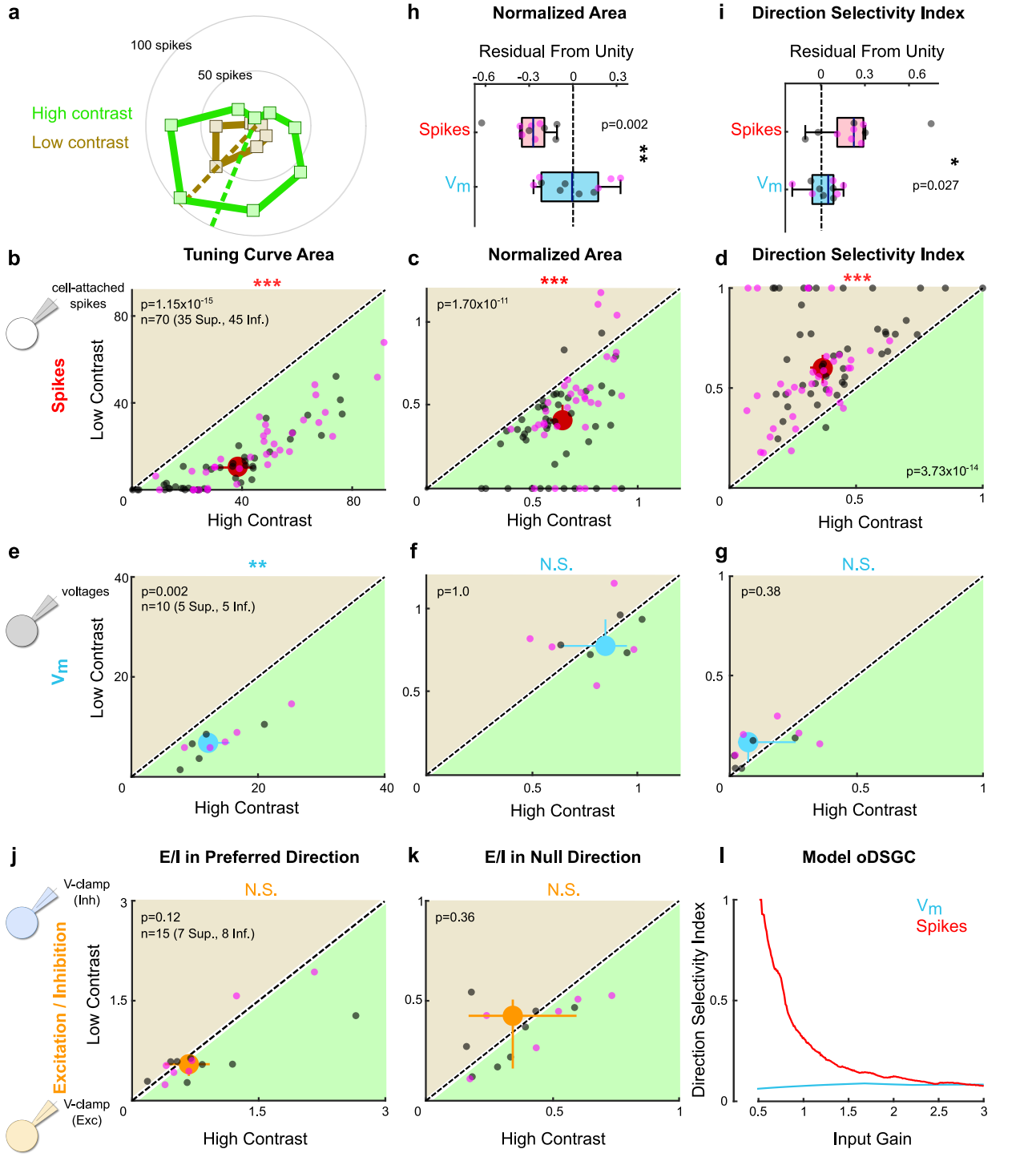
a
100 spikes
50 spikes
High contrast
Low contrast
h
Normalized Area
Residual From Unity
-0.6
-0.3
0
0.3
Spikes
Vm
p=0.002
**
i
Direction Selectivity Index
Residual From Unity
0
0.3
0.6
Spikes
Vm
*
p=0.027
b
Tuning Curve Area
cell-attached spikes
***
p=1.15x10-15
n=70 (35 Sup., 45 Inf.)
Spikes
Low Contrast
High Contrast
c
Normalized Area
***
p=1.70x10-11
High Contrast
d
Direction Selectivity Index
***
p=3.73x10-14
High Contrast
e
voltages
**
p=0.002
n=10 (5 Sup., 5 Inf.)
Vm
Low Contrast
High Contrast
f
N.S.
p=1.0
High Contrast
g
N.S.
p=0.38
High Contrast
j
E/I in Preferred Direction
V-clamp (Inh)
N.S.
p=0.12
n=15 (7 Sup., 8 Inf.)
Excitation / Inhibition
Low Contrast
V-clamp (Exc)
High Contrast
k
E/I in Null Direction
N.S.
p=0.36
High Contrast
l
Model oDSGC
Vm
Spikes
Direction Selectivity Index
Input Gain

Figure 7

1155 **Figure 7. Stimulus contrast modulates the spike tuning curves of oDSGCs. (a)** Example cell-
1156 attached tuning curves from a Superior oDSGC at high (green) and low (tan) contrasts. **(b-d)**
1157 Metrics of **(b)** linear tuning curve area, **(c)** area of the normalized tuning curve, and **(d)** direction
1158 selectivity index from spike responses to high (abscissa) and low (ordinate) contrast bars moving
1159 in 8 directions. The region of tan [or green] indicates the metric is greater under low [or high]
1160 contrast conditions. Points on the line indicate equivalent metrics under the two conditions.
1161 Individual cells are represented by dots. Superior (magenta) and Inferior (gray) oDSGCs maintain
1162 their relative differences even under low contrast (see Fig 2). Red circles represent univariate
1163 medians (collapsed across cell type). Whiskers indicate 95% confidence intervals determined via
1164 bootstrapping. Significance values indicate whether the data tend to fall unevenly on one side of
1165 the unity line (2-sided signed-rank). **(e-g)** Metrics of **(e)** linear tuning curve area, **(f)** area of the
1166 normalized tuning curve, and **(g)** direction selectivity index from subthreshold voltages in
1167 response to high (abscissa) and low (ordinate) contrast bars moving in 8 directions. Blue circles
1168 represent univariate medians (collapsed across cell type). Whiskers indicate 95% confidence
1169 intervals determined via bootstrapping. **(h-i)** Residuals from the unity line for **(h)** area of the
1170 normalized tuning curve and **(i)** direction selectivity index under high and low contrast conditions
1171 for simultaneously measured spikes and subthreshold voltages. Dashed lines indicate unity (i.e.
1172 no difference between high and low contrast). Blue lines represent medians, box boundaries are
1173 IQR, and whiskers represent most extreme observation within 1.5xIQR. Comparisons are made
1174 between spike and Vm distributions (2-sided signed-rank). **(j-k)** E/I ratios for high and low contrast
1175 bars moving in **(j)** the preferred and **(k)** the null direction of each cell. **(l)** Direction selectivity index
1176 generated from a leaky integrate-and-fire model of an oDSGC under different scale factors
1177 applied jointly to excitatory and inhibitory inputs (constant E/I). *$p<0.05$, **$p<0.01$, ***$p<0.001$

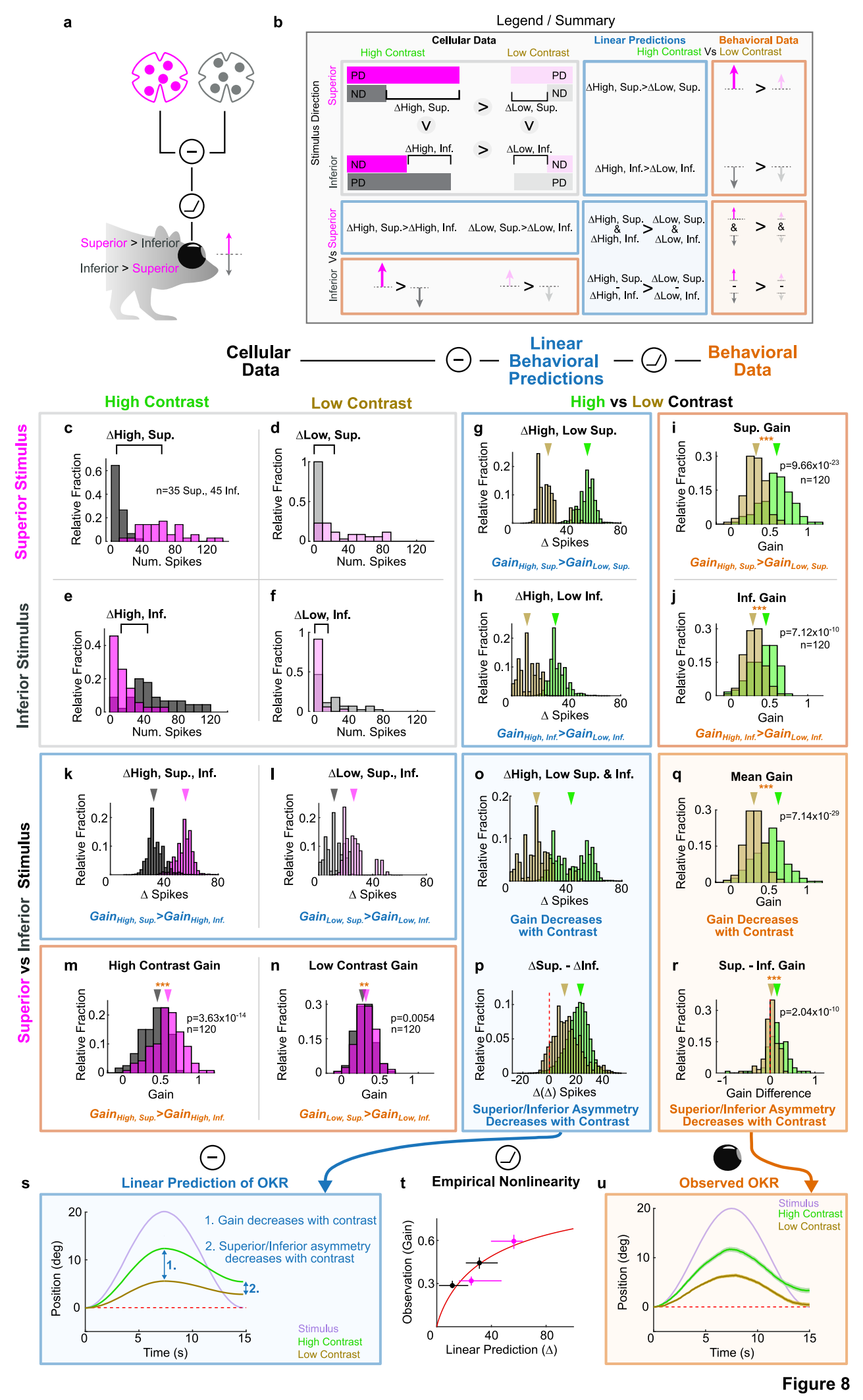
a
Superior > Inferior
Inferior > Superior
b
Legend / Summary
Cellular Data
High Contrast
Low Contrast
Linear Predictions
High Contrast Vs Low Contrast
Behavioral Data
Stimulus Direction
Superior
Inferior
PD
ND
ΔHigh, Sup.
ΔLow, Sup.
ΔHigh, Inf.
ΔLow, Inf.
ΔHigh, Sup.>ΔLow, Sup.
ΔHigh, Inf.>ΔLow, Inf.
Vs Superior
Vs Inferior
ΔHigh, Sup.>ΔHigh, Inf.
ΔLow, Sup.>ΔLow, Inf.
Cellular Data
Linear Behavioral Predictions
Behavioral Data
High Contrast
Low Contrast
High vs Low Contrast
Superior Stimulus
Inferior Stimulus
Superior vs Inferior Stimulus
c ΔHigh, Sup.
n=35 Sup., 45 Inf.
Relative Fraction
Num. Spikes
d ΔLow, Sup.
e ΔHigh, Inf.
f ΔLow, Inf.
g ΔHigh, Low Sup.
Δ Spikes
Gain High, Sup.>Gain Low, Sup.
h ΔHigh, Low Inf.
Gain High, Inf.>Gain Low, Inf.
i Sup. Gain
p=9.66x10-23
n=120
Gain
Gain High, Sup.>Gain Low, Sup.
j Inf. Gain
p=7.12x10-10
n=120
Gain High, Inf.>Gain Low, Inf.
k ΔHigh, Sup., Inf.
Gain High, Sup.>Gain High, Inf.
l ΔLow, Sup., Inf.
Gain Low, Sup.>Gain Low, Inf.
o ΔHigh, Low Sup. & Inf.
Gain Decreases with Contrast
q Mean Gain
p=7.14x10-29
Gain Decreases with Contrast
m High Contrast Gain
p=3.63x10-14
n=120
Gain High, Sup.>Gain High, Inf.
n Low Contrast Gain
p=0.0054
n=120
Gain Low, Sup.>Gain Low, Inf.
p ΔSup. - ΔInf.
Δ(Δ) Spikes
Superior/Inferior Asymmetry Decreases with Contrast
r Sup. - Inf. Gain
p=2.04x10-10
Gain Difference
Superior/Inferior Asymmetry Decreases with Contrast
s Linear Prediction of OKR
1. Gain decreases with contrast
2. Superior/Inferior asymmetry decreases with contrast
Position (deg)
Time (s)
Stimulus
High Contrast
Low Contrast
t Empirical Nonlinearity
Observation (Gain)
Linear Prediction (Δ)
u Observed OKR
Stimulus
High Contrast
Low Contrast
Position (deg)
Time (s)

Figure 8

1178 **Figure 8. Ganglion cell responses predict behavioral OKR gain across stimulus directions**
1179 **and contrasts**. **(a)** Schematic of the putative computation between oDSGCs and OKR, consisting
1180 of a subtraction between Superior and Inferior oDSGC outputs and a nonlinearity. **(b)** Legend and
1181 summary for panels (c-r). Cellular Data (gray box): The responses of Superior (magenta) and
1182 Inferior (gray) oDSGCs in their preferred (PD) and null (ND) directions at high (left column) and
1183 low (right column) contrasts to superior (top row) and inferior (bottom row) drifting stimuli. Linear
1184 predictions (blue boxes): the differences between responses in the preferred and null directions,
1185 represented by Δ, provide predictions of the relative OKR gain for stimuli of different directions
1186 and contrasts. Behavioral results (orange boxes): arrows represent how vertical OKR gain
1187 changes with stimulus direction and contrast. **(c-f)** Cellular Data: Superior (magenta) and Inferior
1188 (gray) oDSGC spike rates for superior (top row) and inferior (bottom row) stimuli at high (left
1189 column) and low (right column) contrast. Brackets above show the difference between the median
1190 responses of the two populations of oDSGCs. **(g-h)** Linear predictions for how behavioral OKR
1191 gain changes across high (green) and low (tan) contrasts for **(g)** superior and **(h)** inferior stimuli.
1192 Predictions are calculated via iteratively bootstrapping the difference of medians from the
1193 distributions shown in (c-f). **(i-j)** Behavioral results of OKR gain for **(i)** superior and **(j)** inferior
1194 motion at high (green) and low (tan) contrast. **(k-l)** Linear predictions for how behavioral OKR gain
1195 changes between superior (magenta) and inferior (gray) stimulus directions at **(k)** high and **(l)** low
1196 contrast. **(m-n)** Behavioral results of OKR gain at **(m)** high and **(n)** low contrast for superior
1197 (magenta) and inferior (gray) stimuli (2-sided signed-rank). **(o)** Linear predictions for behavioral
1198 OKR gain at high (green) and low (tan) contrast, irrespective of stimulus direction. Gain is
1199 predicted to decrease with contrast. **(p)** Linear prediction for how the asymmetry between superior
1200 and inferior OKR changes with contrast. The asymmetry is predicted to be greater at high (green)
1201 compared to low (tan) contrast. **(q)** Behavioral results of OKR gain reveal greater gain at high
1202 (green) compared to low (tan) contrast, irrespective of stimulus direction. **(r)** Behavioral results of
1203 OKR gain reveal that the asymmetry between superior and inferior OKR is greater at high (green)

compared to low (tan) contrast. **(s)** Summary of the linear predictions for eye position across a single stimulus oscillation cycle. Two second-order predictions indicate that (1) gain decreases with contrast and (2) the superior/inferior asymmetry decreases with contrast. **(t)** Relationship between the cellular predictions and the corresponding behavioral OKR gains, i.e. nonlinearity, for superior (magenta points) and inferior (black points) stimuli. Points indicate univariate medians and error bars show 95% confidence intervals determined via bootstrapping. Least-squares fit of a Hill equation to the data (red line), including a maximum value of 1.0 and a fixed point at the origin. **(u)** Summary of behavioral results showing the mean eye position across a single oscillation cycle for high (green, same data as in Fig 1j) and low (tan) contrast oscillating gratings. Stimulus position in lavender. Behavioral OKR shows higher gain and greater asymmetry at high contrast. *$p<0.05$, **$p<0.01$, ***$p<0.001$. See also Fig S6.

REFERENCES

1. Zeil, J., Nalbach, G. & Nalbach, H.-O. Spatial Vision in a Flat World: Optical and Neural Adaptations in Arthropods. in *Neurobiology of Sensory Systems* (eds. Singh, R. N. & Strausfeld, N. J.) 123–137 (Springer US, 1989). doi:10.1007/978-1-4899-2519-0_10.
2. Masseck, O. A. & Hoffmann, K.-P. Comparative Neurobiology of the Optokinetic Reflex. *Ann. N. Y. Acad. Sci.* **1164**, 430–439 (2009).
3. Simpson, J. I. The Accessory Optic System. *Annu. Rev. Neurosci.* **7**, 13–41 (1984).
4. Collewijn, H. Optokinetic eye movements in the rabbit: Input-output relations. *Vision Res.* **9**, 117–132 (1969).
5. Donaghy, M. The contrast sensitivity, spatial resolution and velocity tuning of the cat's optokinetic reflex. *J. Physiol.* **300**, 353–365 (1980).
6. Gravot, C. M., Knorr, A. G., Glasauer, S. & Straka, H. It's not all black and white: visual scene parameters influence optokinetic reflex performance in Xenopus laevis tadpoles. *J. Exp. Biol.* **220**, 4213–4224 (2017).
7. Knorr, A. G., Gravot, C. M., Glasauer, S. & Straka, H. Image motion with color contrast suffices to elicit an optokinetic reflex in Xenopus laevis tadpoles. *Sci. Rep.* **11**, 8445 (2021).
8. Leguire, L. E. *et al.* Contrast sensitivity of optokinetic nystagmus. *Vision Res.* **31**, 89–97 (1991).
9. Cahill, H. & Nathans, J. The Optokinetic Reflex as a Tool for Quantitative Analyses of Nervous System Function in Mice: Application to Genetic and Drug-Induced Variation. *PLOS ONE* **3**, e2055 (2008).
10. Dehmelt, F. A. *et al.* Spherical arena reveals optokinetic response tuning to stimulus location, size, and frequency across entire visual field of larval zebrafish. *eLife* **10**, e63355 (2021).
11. Shimizu, N. *et al.* Distribution of optokinetic sensitivity across the retina of mice in relation to

eye orientation. *Neuroscience* **168**, 200–208 (2010).

12. Dhande, O. S., Stafford, B. K., Lim, J.-H. A. & Huberman, A. D. Contributions of Retinal Ganglion Cells to Subcortical Visual Processing and Behaviors. *Annu. Rev. Vis. Sci.* **1**, 291–328 (2015).
13. Giolli, R. A., Blanks, R. H. I. & Lui, F. The accessory optic system: basic organization with an update on connectivity, neurochemistry, and function. in *Progress in Brain Research* (ed. Büttner-Ennever, J. A.) vol. 151 407–440 (Elsevier, 2006).
14. Oyster, C. W. The analysis of image motion by the rabbit retina. *J. Physiol.* **199**, 613–635 (1968).
15. Oyster, C. W. & Barlow, H. B. Direction-Selective Units in Rabbit Retina: Distribution of Preferred Directions. *Science* **155**, 841–842 (1967).
16. Sabbah, S. *et al.* A retinal code for motion along the gravitational and body axes. *Nature* **546**, 492–497 (2017).
17. Dhande, O. S. *et al.* Genetic Dissection of Retinal Inputs to Brainstem Nuclei Controlling Image Stabilization. *J. Neurosci.* **33**, 17797–17813 (2013).
18. Lilley, B. N. *et al.* Genetic access to neurons in the accessory optic system reveals a role for Sema6A in midbrain circuitry mediating motion perception. *J. Comp. Neurol.* **527**, 282–296 (2019).
19. Sun, L. O. *et al.* Functional Assembly of Accessory Optic System Circuitry Critical for Compensatory Eye Movements. *Neuron* **86**, 971–984 (2015).
20. Yonehara, K. *et al.* Expression of SPIG1 Reveals Development of a Retinal Ganglion Cell Subtype Projecting to the Medial Terminal Nucleus in the Mouse. *PLoS ONE* **3**, (2008).
21. Yonehara, K. *et al.* Identification of Retinal Ganglion Cells and Their Projections Involved in Central Transmission of Information about Upward and Downward Image Motion. *PLoS ONE* **4**, (2009).
22. Togt, C. van der, Want, J. van der & Schmidt, M. Segregation of direction selective neurons

and synaptic organization of inhibitory intranuclear connections in the medial terminal nucleus of the rat: An electrophysiological and immunoelectron microscopical study. *J. Comp. Neurol.* **338**, 175–192 (1993).

23. Kay, J. N. *et al.* Retinal Ganglion Cells with Distinct Directional Preferences Differ in Molecular Identity, Structure, and Central Projections. *J. Neurosci.* **31**, 7753–7762 (2011).
24. Osterhout, J. A., Stafford, B. K., Nguyen, P. L., Yoshihara, Y. & Huberman, A. D. Contactin-4 Mediates Axon-Target Specificity and Functional Development of the Accessory Optic System. *Neuron* **86**, 985–999 (2015).
25. Pak, M. W. *et al.* Retinopretectal and accessory optic projections of normal mice and the OKN-defective mutant mice beige, beige-J, and pearl. *J. Comp. Neurol.* **258**, 435–446 (1987).
26. Oyster, C. W., Takahashi, E. & Collewijn, H. Direction-selective retinal ganglion cells and control of optokinetic nystagmus in the rabbit. *Vision Res.* **12**, 183–193 (1972).
27. Wei, W. Neural Mechanisms of Motion Processing in the Mammalian Retina. *Annu. Rev. Vis. Sci.* **4**, 165–192 (2018).
28. Takahashi, M., Sakurai, S. & Kanzaki, J. Horizontal and Vertical Optokinetic Nystagmus in Man. *ORL J Otorhinolaryngol Relat Spec* **40**, 43–52 (1978).
29. Hainline, L., Lemerise, E., Abramov, I. & Turkel, J. Orientational asymmetries in small-field optokinetic nystagmus in human infants. *Behav. Brain Res.* **13**, 217–230 (1984).
30. Murasugi, C. M. & Howard, I. P. Up-down asymmetry in human vertical optokinetic nystagmus and afternystagmus: contributions of the central and peripheral retinae. *Exp. Brain Res.* **77**, 183–192 (1989).
31. van den Berg, A. V. & Collewijn, H. Directional asymmetries of human optokinetic nystagmus. *Exp. Brain Res.* **70**, 597–604 (1988).
32. Knapp, C. M., Proudlock, F. A. & Gottlob, I. OKN Asymmetry in Human Subjects: A Literature Review. *Strabismus* **21**, 37–49 (2013).

33. Hoffmann, K.-P. & Fischer, W. H. Directional effect of inactivation of the nucleus of the optic tract on optokinetic nystagmus in the cat. *Vision Res.* **41**, 3389–3398 (2001).
34. Evinger, C. & Fuchs, A. F. Saccadic, smooth pursuit, and optokinetic eye movements of the trained cat. *J. Physiol.* **285**, 209–229 (1978).
35. Grasse, K. L. & Cynader, M. S. The effect of visual cortex lesions on vertical optokinetic nystagmus in the cat. *Brain Res.* **455**, 385–389 (1988).
36. Wallman, J. & Velez, J. Directional asymmetries of optokinetic nystagmus: developmental changes and relation to the accessory optic system and to the vestibular system. *J. Neurosci.* **5**, 317–329 (1985).
37. Takahashi, M. & Igarashi, M. Comparison of Vertical and Horizontal Optokinetic Nystagmus in the Squirrel Monkey. *ORL* **39**, 321–329 (1977).
38. Denman, D. J., Siegle, J. H., Koch, C., Reid, R. C. & Blanche, T. J. Spatial Organization of Chromatic Pathways in the Mouse Dorsal Lateral Geniculate Nucleus. *J. Neurosci.* **37**, 1102–1116 (2017).
39. Yonehara, K. *et al.* Congenital Nystagmus Gene FRMD7 Is Necessary for Establishing a Neuronal Circuit Asymmetry for Direction Selectivity. *Neuron* **89**, 177–193 (2016).
40. Briggman, K. L., Helmstaedter, M. & Denk, W. Wiring specificity in the direction-selectivity circuit of the retina. *Nature* **471**, 183–188 (2011).
41. Fried, S. I., Münch, T. A. & Werblin, F. S. Mechanisms and circuitry underlying directional selectivity in the retina. *Nature* **420**, 411–414 (2002).
42. Wei, W., Hamby, A. M., Zhou, K. & Feller, M. B. Development of asymmetric inhibition underlying direction selectivity in the retina. *Nature* **469**, 402–406 (2011).
43. Ding, H., Smith, R. G., Poleg-Polsky, A., Diamond, J. S. & Briggman, K. L. Species-specific wiring for direction selectivity in the mammalian retina. *Nature* **535**, 105–110 (2016).
44. Amthor, F. R., Keyser, K. T. & Dmitrieva, N. A. Effects of the destruction of starburst-cholinergic amacrine cells by the toxin AF64A on rabbit retinal directional selectivity. *Vis.*

Neurosci. **19**, 495–509 (2002).

45. Yonehara, K. *et al.* Spatially asymmetric reorganization of inhibition establishes a motion-sensitive circuit. *Nature* **469**, 407–410 (2011).
46. Yoshida, K. *et al.* A Key Role of Starburst Amacrine Cells in Originating Retinal Directional Selectivity and Optokinetic Eye Movement. *Neuron* **30**, 771–780 (2001).
47. Mauss, A. S., Vlasits, A., Borst, A. & Feller, M. Visual Circuits for Direction Selectivity. *Annu. Rev. Neurosci.* **40**, 211–230 (2017).
48. Vaney, D. I., Sivyer, B. & Taylor, W. R. Direction selectivity in the retina: symmetry and asymmetry in structure and function. *Nat. Rev. Neurosci.* **13**, 194–208 (2012).
49. Mani, A. *et al. A retinal circuit that vetoes optokinetic responses to fast visual motion*. http://biorxiv.org/lookup/doi/10.1101/2021.10.31.466688 (2021) doi:10.1101/2021.10.31.466688.
50. Matsumoto, A., Briggman, K. L. & Yonehara, K. Spatiotemporally Asymmetric Excitation Supports Mammalian Retinal Motion Sensitivity. *Curr. Biol.* **29**, 3277-3288.e5 (2019).
51. Koulen, P., Fletcher, E. L., Craven, S. E., Bredt, D. S. & Wässle, H. Immunocytochemical Localization of the Postsynaptic Density Protein PSD-95 in the Mammalian Retina. *J. Neurosci.* **18**, 10136–10149 (1998).
52. Sassoè-Pognetto, M. *et al.* Colocalization of gephyrin and GABAA-receptor subunits in the rat retina. *J. Comp. Neurol.* **357**, 1–14 (1995).
53. Sassoè-Pognetto, M. & Wässle, H. Synaptogenesis in the rat retina: subcellular localization of glycine receptors, GABAA receptors, and the anchoring protein gephyrin. *J. Comp. Neurol.* **381**, 158–174 (1997).
54. Matsumoto, A. *et al.* Direction selectivity in retinal bipolar cell axon terminals. *Neuron* **0**, (2021).
55. Percival, K. A., Venkataramani, S., Smith, R. G. & Taylor, W. R. Directional excitatory input to direction-selective ganglion cells in the rabbit retina. *J. Comp. Neurol.* **527**, 270–281

(2019).

56. Poleg-Polsky, A. & Diamond, J. S. Imperfect Space Clamp Permits Electrotonic Interactions between Inhibitory and Excitatory Synaptic Conductances, Distorting Voltage Clamp Recordings. *PLOS ONE* **6**, e19463 (2011).
57. Summers, M. T. & Feller, M. B. Distinct inhibitory pathways control velocity and directional tuning in the mouse retina. *Curr. Biol.* **0**, (2022).
58. Yonehara, K. *et al.* The First Stage of Cardinal Direction Selectivity Is Localized to the Dendrites of Retinal Ganglion Cells. *Neuron* **79**, 1078–1085 (2013).
59. Oesch, N., Euler, T. & Taylor, W. R. Direction-Selective Dendritic Action Potentials in Rabbit Retina. *Neuron* **47**, 739–750 (2005).
60. Poleg-Polsky, A. & Diamond, J. S. NMDA Receptors Multiplicatively Scale Visual Signals and Enhance Directional Motion Discrimination in Retinal Ganglion Cells. *Neuron* **89**, 1277–1290 (2016).
61. Poleg-Polsky, A. & Diamond, J. S. Retinal Circuitry Balances Contrast Tuning of Excitation and Inhibition to Enable Reliable Computation of Direction Selectivity. *J. Neurosci.* **36**, 5861–5876 (2016).
62. Sethuramanujam, S. *et al.* A Central Role for Mixed Acetylcholine/GABA Transmission in Direction Coding in the Retina. *Neuron* **90**, 1243–1256 (2016).
63. Sethuramanujam, S. *et al.* “Silent” NMDA Synapses Enhance Motion Sensitivity in a Mature Retinal Circuit. *Neuron* **96**, 1099-1111.e3 (2017).
64. Soodak, R. E. & Simpson, J. I. The accessory optic system of rabbit. I. Basic visual response properties. *J. Neurophysiol.* **60**, 2037–2054 (1988).
65. Giolli, R. A. *et al.* GABAergic neurons comprise a major cell type in rodent visual relay nuclei: an immunocytochemical study of pretectal and accessory optic nuclei. *Exp. Brain Res.* **61**, 194–203 (1985).
66. Grasse, K. L. & Cynader, M. S. Electrophysiology of medial terminal nucleus of accessory

optic system in the cat. *J. Neurophysiol.* **48**, 490–504 (1982).

67. Natal, C. L. & Britto, L. R. G. The rat accessory optic system: effects of cortical lesions on the directional selectivity of units within the medial terminal nucleus. *Neurosci. Lett.* **91**, 154–159 (1988).
68. Simpson, J. I., Soodak, R. E. & Hess, R. The Accessory Optic System and its Relation to the Vestibulocerebellum. in *Progress in Brain Research* (eds. Granit, R. & Pompeiano, O.) vol. 50 715–724 (Elsevier, 1979).
69. Mowrer, O. H. A comparison of the reaction mechanisms mediating optokinetic nystagmus in human beings and in pigeons. *Psychol. Monogr.* **47**, 294–305 (1936).
70. Liu, B., Huberman, A. D. & Scanziani, M. Cortico-fugal output from visual cortex promotes plasticity of innate motor behaviour. *Nature* **538**, 383–387 (2016).
71. Wood, C. C., Spear, P. D. & Braun, J. J. Direction-specific deficits in horizontal optokinetic nystagmus following removal of visual cortex in the cat. *Brain Res.* **60**, 231–237 (1973).
72. Cook, J. E. & Podugolnikova, T. A. Evidence for spatial regularity among retinal ganglion cells that project to the accessory optic system in a frog, a reptile, a bird, and a mammal. *Vis. Neurosci.* **18**, 289–297 (2001).
73. Dann, J. F. & Buhl, E. H. Retinal ganglion cells projecting to the accessory optic system in the rat. *J. Comp. Neurol.* **262**, 141–158 (1987).
74. Ruff, T. *et al.* FLRT3 Marks Direction-Selective Retinal Ganglion Cells That Project to the Medial Terminal Nucleus. *Front. Mol. Neurosci.* **14**, (2021).
75. Tauber, E. S. & Atkin, A. Optomotor Responses to Monocular Stimulation: Relation to Visual System Organization. *Science* **160**, 1365–1367 (1968).
76. Holmgren, C. D. *et al.* Visual pursuit behavior in mice maintains the pursued prey on the retinal region with least optic flow. *eLife* **10**, e70838 (2021).
77. Lee, S. *et al.* An unconventional glutamatergic circuit in the retina formed by vGluT3 amacrine cells. *Neuron* **84**, 708–715 (2014).

78. Sivyer, B., Tomlinson, A. & Taylor, W. R. Simulated Saccadic Stimuli Suppress ON-Type Direction-Selective Retinal Ganglion Cells via Glycinergic Inhibition. *J. Neurosci.* **39**, 4312–4322 (2019).

79. Kittila, C. A. & Massey, S. C. Pharmacology of Directionally Selective Ganglion Cells in the Rabbit Retina. *J. Neurophysiol.* **77**, 675–689 (1997).

80. Carandini, M. & Heeger, D. J. Normalization as a canonical neural computation. *Nat. Rev. Neurosci.* **13**, 51–62 (2012).

81. Barlow, H. B. Summation and inhibition in the frog's retina. *J. Physiol.* **119**, 69–88 (1953).

82. Hartline, H. K., Wagner, H. G. & MacNichol, E. F. The Peripheral Origin of Nervous Activity in the Visual System. *Cold Spring Harb. Symp. Quant. Biol.* **17**, 125–141 (1952).

83. Kuffler, S. W. Discharge patterns and functional organization of mammalian retina. *J. Neurophysiol.* **16**, 37–68 (1953).

84. Dacey, D. M., Crook, J. D. & Packer, O. S. Distinct synaptic mechanisms create parallel S-ON and S-OFF color opponent pathways in the primate retina. *Vis. Neurosci.* **31**, 139–151 (2014).

85. De Monasterio, F. M. & Gouras, P. Functional properties of ganglion cells of the rhesus monkey retina. *J. Physiol.* **251**, 167–195 (1975).

86. Field, G. D. *et al.* High-sensitivity rod photoreceptor input to the blue-yellow color opponent pathway in macaque retina. *Nat. Neurosci.* **12**, 1159–1164 (2009).

87. Suver, M. P. *et al.* Encoding of Wind Direction by Central Neurons in Drosophila. *Neuron* **102**, 828-842.e7 (2019).

88. Martin, H. Osmotropotaxis in the Honey-Bee. *Nature* **208**, 59–63 (1965).

89. Schwenk, K. Why snakes have forked tongues. *Science* **263**, 1573 (1994).

90. Middlebrooks, J. C. & Green, D. M. Sound Localization by Human Listeners. *Annu. Rev. Psychol.* **42**, 135–159 (1991).

91. Stahl, J. S., van Alphen, A. M. & De Zeeuw, C. I. A comparison of video and magnetic

search coil recordings of mouse eye movements. *J. Neurosci. Methods* **99**, 101–110 (2000).

92. Stahl, J. S. Eye Movements of the Murine P/Q Calcium Channel Mutant Rocker, and the Impact of Aging. *J. Neurophysiol.* **91**, 2066–2078 (2004).
93. Zoccolan, D., Graham, B. J. & Cox, D. D. A Self-Calibrating, Camera-Based Eye Tracker for the Recording of Rodent Eye Movements. *Front. Neurosci.* **4**, 193 (2010).
94. Rodieck, R. W. The density recovery profile: A method for the analysis of points in the plane applicable to retinal studies. *Vis. Neurosci.* **6**, 95–111 (1991).
95. Care, R. A. *et al.* Partial Cone Loss Triggers Synapse-Specific Remodeling and Spatial Receptive Field Rearrangements in a Mature Retinal Circuit. *Cell Rep.* **27**, 2171-2183.e5 (2019).
96. Care, R. A. *et al.* Mature Retina Compensates Functionally for Partial Loss of Rod Photoreceptors. *Cell Rep.* **31**, (2020).
97. Remtulla, S. & Hallett, P. E. A schematic eye for the mouse, and comparisons with the rat. *Vision Res.* **25**, 21–31 (1985).
98. Antoine, M. W., Langberg, T., Schnepel, P. & Feldman, D. E. Increased Excitation-Inhibition Ratio Stabilizes Synapse and Circuit Excitability in Four Autism Mouse Models. *Neuron* **101**, 648-661.e4 (2019).